AFOSR-TR-97-0455

REPORT DOCUMENTATION PAGE

Form Approved
OMB No. 0704-0188

1. AGENCY USE ONLY (Leave blank)	2. REPORT DATE January 1997	3. REPORT TYPE AND DATES COVERED Final Technical : June 93 – Nov. 96

4. TITLE AND SUBTITLE

Fracture characteristics of fiber composites

5. FUNDING NUMBERS

6. AUTHOR(S)

John Botsis

93 - 1 - 0319

7. PERFORMING ORGANIZATION NAME(S) AND ADDRESS(ES)

Department of Civil Engineering,
Mechanics and Metallurgy (mc 246)
University of Illinois, Chicago
842 W Taylor Str. Chicago IL 60607

8. PERFORMING ORGANIZATION REPORT NUMBER

9. SPONSORING/MONITORING AGENCY NAME(S) AND ADDRESS(ES)

Air Force Office of Scientific Research
Aerospace and Engineering Sciences
Building 410, Bolling AFB
Washington D.C. 20332

10. SPONSORING/MONITORING AGENCY REPORT NUMBER

N/A

11. SUPPLEMENTARY NOTES

N/A

19971006 035

12a. DISTRIBUTION/AVAILABILITY STATEMENT

Approved for public release;
Distribution unlimited

...ION CODE

N/A

13. ABSTRACT (Maximum 200 words)

Investigations of the effects of fiber spacing on the mechanical properties and strength of a model composite system with well aligned and uniformly spaced fibers are reported. Monolayer and multilayer fiber architectures were investigated. For the monolayer fiber architecture specimens, strength, σ_c, depended on the fiber spacing, λ, according to $\sigma_c = \kappa/\sqrt{\lambda}$ where κ is a constant related to the matrix properties. The linear portion of the stress-strain curves 'collapsed' when multiplied by the term $\sqrt{\lambda}/\sqrt{w}$, where w is the specimen width. Acoustic emission indicated that the non-linear stress-strain behavior was coincided with activity at the fiber-matrix interface. For the multilayer fiber architecture, strength was found to depend on fiber spacing in the form, $\sigma_c = \kappa/\sqrt{\lambda_x} + \sigma_o$ where σ_o was an intercept of undetermined origin. No scaling of any portion of the load-displacement curves was observed. For this fiber architecture the stiffness of the specimens decreased with a decrease in fiber spacing while the toughness increased with a decrease in fiber spacing. This behavior was directly related to the increase in fiber-matrix interface area that accompanied the decrease in fiber spacing. A boundary element algorithm was used to investigate the stress intensity factor of a 2-dimensional representation of the reinforced specimens. Good correlation was found between the numerical and experimental results.

14. SUBJECT TERMS

composites; fiber spacing; strength; mechanical responce

15. NUMBER OF PAGES 81

16. PRICE CODE

17. SECURITY CLASSIFICATION OF REPORT	18. SECURITY CLASSIFICATION OF THIS PAGE	19. SECURITY CLASSIFICATION OF ABSTRACT	20. LIMITATION OF ABSTRACT
UNCLASSIFIED	UNCLASSIFIED	UNCLASSIFIED	

DTIC QUALITY INSPECTED 3

FRACTURE CHARACTERISTICS OF FIBER COMPOSITES

FINAL REPORT

January 1997

by

John Botsis, Professor

Department of Civil
and Materials Engineering
2095 ERF, 842 W. Taylor Str.
University of Illinois at Chicago,
Chicago, IL 60607

present address
Laboratory of Applied Mechanics/IMECO
Department of Mechanical Engineering
Swiss Federal Institute of Technology
CH -1015, LAUSANNE, SWITZERLAND
Voice: ++41 21 693 29 69
secretary   ++41 21 693 29 37
Fax: ++41 21 693 35 09
e-mail: john.botsis@imeco.dgm.epfl.ch

prepared for

SUMMARY

This work was set to investigate the effects of fiber spacing on the mechanical properties and strength of a model composite system with long well aligned fibers. Two fiber architectures were investigated:

1. a 'monolayer' fiber architecture in which the fiber spacing varied from specimen to specimen. Uniaxial tension experiments were performed on notched and unnotched specimens to examine the stress-strain response and the fracture properties.

2. a 'multilayer' fiber array in which the fiber spacing in one direction was constant while the fiber spacing in the second direction was varied from specimen to specimen. Compact tension specimens were used to investigate the load-displacement response and fracture behavior.

The experimental results on strength and fracture of the multilayer architecture were modeled numerically using a Boundary Element Method algorithm.

Although the results reported in this paper and elsewhere are on a model composite system, they can provide a sound knowledge base for a better understanding of crack bridging in composites materials. In particular, for systems where it is not realistic to use a continuum approximation of the reinforcement in the bridging zone and ahead of the crack tip, the results of such studies can be very useful in understanding the influence of various length parameters. Furthermore it is the authors belief that results of studies in model composites can provide an important supplement to efforts aimed at predicting the response of real composite materials.

IMPORTANT FINDINGS

For the monolayer fiber architecture specimens, strength, σ_c, was found to depend on the inverse root of the fiber spacing, λ, according to $\sigma_c = \kappa/\sqrt{\lambda}$ where κ is a constant related to the matrix properties. The elastic behavior of these specimens was also found to depend on fiber spacing, i.e. the linear portion of the stress-strain curves 'collapsed' when multiplied by the term $\sqrt{\lambda}/\sqrt{w}$, where w is the specimen width. The stiffness of the specimens increased with a decrease in fiber spacing and through the use of acoustic emission methods, non-linear stress-strain behavior was found to coincide with damage of the fiber-matrix interface.

For the multilayer fiber architecture, strength was also found to depend on fiber spacing but with a slightly different function, i.e. $\sigma_c = \kappa/\sqrt{\lambda_x} + \sigma_o$ where σ_o was a y-intercept of undetermined origin. No scaling of any portion of the stress-strain curves was observed. For this fiber architecture the stiffness of the specimens decreased with a decrease in fiber spacing while the toughness increased with a decrease in fiber spacing. This behavior was directly related to the increase in fiber-matrix interface area that accompanied the decrease in fiber spacing. Through the coupling of acoustic emission methods with in-situ crack-tip observations, the onset of non-linear stress-strain behavior in these specimens was found to coincide with crack tip extension as well as fiber-matrix interface damage.

The BEM algorithm was used to investigate the crack tip stress behavior of a 2-dimensional representation of the reinforced compact tension specimens. Good correlation was found between the numerically modeled crack tip stress and the experimental stress at the onset of crack growth.

TABLE OF CONTENTS

LIST OF TABLES

LIST OF FIGURES

LIST OF FIGURES (continued)

LIST OF ABBREVIATIONS

ACK   Aveston, Cooper and Kelly

ASTM   American Society for Testing and Materials

BEM   Boundary Element Method

CT   Compact Tension

FEM   Finite Element Method

LEFM   Linear Elastic Fracture Mechanics

ROM   Rule of Mixtures

SIF   Stress Intensity Factor

1 INTRODUCTION

1.1 Motivation

Composites are becoming an increasingly important class of material. From state of the art aircraft to tennis rackets, composites are finding their way into all areas of engineering. What makes composites so desirable are their specific properties, i.e. property to weight ratios, and the ability to tailor make a material with properties superior to either of the constituent materials.

Yet, unlike common engineering materials such as steel, glass and concrete, the behavior of composites are still not well understood. It is, however, well established that damage processes in composites, such as micro-cracking of the matrix, fiber-bridging and fiber debonding, sliding and pull-out, play major roles in energy absorption, hence increase the toughness. Still, the evolution and relative importance of these processes are the subject of intense research.

Even less well understood are the parameters controlling strength in composites. This is a major limitation in the use of composites for engineering applications. The importance of understanding the strength behavior of a material is illustrated in the application of the engineering materials previously mentioned. For example, quality control of steel parts includes microstructural evaluation of only a small number of the parts from a given lot. This is due to the ability to predict a steel's strength based on its microstructure, specifically, by measuring its grain size. It is known that the strength of brittle materials, e.g. glass, are limited by a critical flaw size. The strength of concrete can also be predicted based on a microstructural characteristic, pore size. Astonishing then, perhaps, is the lack of models which can give quantitative predictions of composite strength based on its microstructure.

While there have been many attempts to correlate the strength of a composite to it's microstructure, a model which can relate strength to a single characteristic scale does not exist. Most strength models neglect the exact distribution of fibers, instead using the 'generic' volume fraction term to relate the composite strength to fiber diameter, interfacial strength and other parameters. However, fiber distribution is rarely considered. A model which could predict the strength of a composite based on a characteristic length of the fiber architecture would be a great step forward in the understanding and application of composites.

One way to investigate scale effects is to vary the specimen geometry in an appropriate manner. Another way is to maintain the specimen size the same and change the morphology (i.e., fiber spacing, grain or pore size) of the material in a controlled way. The latter approach may be useful in systems with characteristic morphological features. In this work, results of longitudinal strength on a specially made composite material are reported. The composite consisted of one or more layers of well - aligned fibers. The primary objective of the work reported herein was to relate the composite's loading response and strength with fiber spacing. Strength data were treated with the rule of mixture as well as with dimensional analysis arguments.

1.2 Review

There are three general classes of composites; ceramic-, metal- and polymer-matrix composites. There are also many, if not hundreds, of ways to construct the reinforcing fiber architecture (Ko, 1989; Prewo, 1989). Even the reinforcing fibers, from glass to carbon to Kevlar, and forms of these fibers, from short to continuous fibers and random to aligned to woven fiber orientations, are vast. The work presented here is exclusively concerned with a single polymer matrix reinforced with a monofilament glass fiber. In each case the reinforcing 'fibers' were continuous and aligned in the loading direction. The strength and fracture behavior as a function of the fiber spacing was studied. Therefore the subsequent review is dedicated to relevant work on similar systems.

1

Strength may be the final or most extreme value which can describe the load bearing capacity of a composite (Rosen, 1964), or any material. From the synthesis of a composite one typically hopes to retain strength of the matrix while adding toughness via the reinforcing fibers as in a ceramic matrix composite, or conversely, to give a flexible matrix strength as in polymer matrix composites. However, it is important to realize that the many energy absorbing processes which give a composite toughness, including matrix and fiber cracking, fiber sliding and pull-out, delamination and even plastic deformation, may also have profound implications on the strength of the composite (Kerans et al., 1989; Shah and Ouyang, 1991; Aveston et al., 1971). Yet, a model which can predict strength of a composite as a function of the reinforcing fibers (with minimal as well as easy to measure parameters) has been difficult to formulate for composite materials.

Perhaps the first model to express composite strength as a function of the reinforcing fibers was the rule of mixtures, ROM. This model attempted to predict a composite's strength based on the ultimate stress, or strain, of the constituent materials and their volume fractions. It was quickly realized that in a typical composite only one of the constituents actually reaches it's ultimate stress, or strain, at composite failure while the other constituent has not yet reached it's load bearing capacity. The ROM was then modified to handle the two possible relationships between the fiber and matrix ultimate properties. First, a matrix with a greater strain to failure than the fibers and second, fibers with a greater strain to failure than the matrix. As early as the mid sixties, investigators (Broutman and Krock, 1967) were finding that the ROM, while accurate for predicting the composite's Young's modulus, was inaccurate for calculating strength in many cases. Rosen had already begun to describe the research community's realization that different failure mechanisms existed for different systems. He proposed a model based on the weakest link theory of the fibers combined with the fiber volume fraction. Since then authors have continuously shown, and explained why, the ROM is the exception rather than the rule even for uniaxially reinforced composites using the iso-strain conditions on which the model was based (Warren and Sarin, 1989).

Aveston, Cooper and Kelly, ACK, were among the first investigators to look critically at the ROM as a model for strength prediction and propose an alternate model (Aveston et al., 1971). For uniaxially aligned composites they addressed both cases of the strain to failure relationship between the fiber and matrix. Using the shear lag analysis model for stress transfer between the matrix and the fiber (Corten, 1967) they proposed a model to predict the failure morphology of the specimen based on measurable system parameters. Furthermore, they used energy balance arguments to predict composite strength and showed that the presence of a reinforcing material alters the ultimate properties of the matrix therefore limiting the validity of the ROM for strength predictions.

Based on the ACK model, Marshall, Cox and Evans, MCE, took a closer look at the 'first' matrix crack which typically defines composite strength in brittle matrix systems, (Marshall et al., 1985). This work assumed that a critical flaw will cause matrix cracking, revealed by non-linearity of the stress strain curve, before the failure point used by the ACK model. The model of MCE used stress intensity factor, SIF, methods to model crack growth of long bridged cracks and short cracks with no fiber bridging.

A third model by Budiansky, Hutchinson and Evans, BHE, followed in the footsteps of the previous two works (Budiansky et al., 1986). Again, this model was based on the original ACK model but with different interfacial conditions, i.e. purely frictional fiber-matrix interfaces and weakly bonded fiber matrix interfaces.

While all three of the previously mentioned models, ACK, MCE and BHE, give experimental evidence to back up their respective models, there have also been attempts to model composite strength based solely on numerical investigations. Rubinstein (1993) used a SIF approach along with fiber bridging, fiber spacing and toughness parameters to predict crack growth. Crack arrest has been modeled numerically based on the energy dissipation of sliding fibers bridging the crack (Shibata et al., 1988). The use of SIF and energy release rate, from linear

2

elastic fracture mechanics, LEFM, are often used in research dedicated to the understanding of delamination and crack growth in composite materials (Johannesson and Blikstad, 1985; Davidson, 1994; Kardomateas et al., 1994; Beldica, 1996).

A common theme to all of the above models, is that the influence of the fibers on the crack is only considered after a crack has propagated past the fibers and the fibers are able to bridge the crack. This allows energy dissipation through fiber sliding and/or debonding. Very few authors have addressed the effect of fibers on crack propagation for fibers which lie in the uncracked matrix ahead of the crack tip. The earliest consideration of this type may have been by Parikh (1964) who showed that fiber distance in uniaxially aligned short fiber metal matrix composites resulted in a Orowan-Petch type relationship (Kingery et al., 1976), i.e. square root of end-to-end fiber spacing was the controlling parameter. Similarly, Wagner (1989) discussed a Griffith type dependence on strength based on the square root of fiber diameter.

Recently, new models have returned to the idea that some characteristic length can be used to predict composite strength. These authors (Botsis et al., 1994; Botsis et al., 1995; Zhao, 1995) have proposed center-to-center fiber spacing as a characteristic strength for uniaxial continuously reinforced composites. For polymer matrix composites, attempts to correlate the shear and tensile bands ahead of the crack tip to strength have been made (Sou et al., 1994). This latter work is interesting due to the possible relationships among fiber spacing, shear band formation and fracture mechanics.

To understand the processes that control strength and toughness, i.e. damage processes, in composites many techniques have been used. Perhaps the most prevalent method is the monitoring of stress waves released by damage processes which occur during loading. These stress waves are in the acoustic range, and hence are referred to as 'acoustic emissions', AE. A review of specific testing capabilities using AE methods is given by Vahaviolos (1995). One of the most important results to come from the use of AE methods was revealed by (Kim and Pagano, 1991) and also noted by (Czigany and Karger-Kocsis, 1993). In these works it was shown that initial matrix cracking in brittle systems and damage at the fiber-matrix interface, respectively, occur before the onset of stress-strain non-linearity. Therefore, the use of the proportional limit as an indication of crack initiation or growth may in fact overestimate the true critical stress.

It is common practice to separate acoustic emission events into low-, mid-, and high-amplitude or energy events corresponding to matrix cracking, delamination or debonding and fiber fracture, respectively, (Sundaresan and E.G. Henneke II, 1988). However, it has been shown that AE signals are relative to each particular test set-up and unless the system is specifically calibrated, in general one cannot be sure of the acoustic emission sources, (Daniel, 1993). In addition, acoustic signals generated by friction can cause false signals in the form of 'event trains' and must be filtered out before conclusions on the presence and signature of other processes can be made, (Cohen and Awerbuch, 1988).

Even if calibration is performed, the task of separating simultaneous AE signals is monumental at best, requiring highly specialized equipment (Bouden et al., 1995). Under ideal conditions, AE data can indicate regimes of various damage processes through changes in the AE signal characteristic (Priston et al., 1995). According to Vahaviolos, energy is the best indicator of various damage processes but also the most difficult to measure. Therefore, as one might expect, the characteristic easiest to measure, i.e. AE count rate and/or cumulative counts, has become the traditional AE parameter for reporting and describing damage in composites.

Of course visual methods, when applicable, are invaluable for correlating damage processes 'suggested' by other methods to observed processes. Photoelastic methods are still widely used along with both in-situ high-speed video recording (Rosakis et al., 1994), SEM observations (Sundaresan and Henneke II, 1988) and light microscopy. Other methods for damage investigation of composites structures include in-situ electric resistance measurements, thermography and radiography.

3

Finally, dimensional analysis has been the basis for the explanation of many physical phenomenon, even those which have proven to be very complex, for instance fluid flow (Barrenblatt, 1987). Although the concept of dimensional analysis is itself simplistic, it is powerful and can give an investigator a new or fresh view of his or her approach that can greatly add to the understanding of the phenomenon being investigated.

1.3 Definitions

As stated previously the aim of this work is to describe the strength and fracture of a model composite system. Yet with the advent of composite materials and fracture mechanics the explanations of these intuitive concepts have become very system specific. In this section, a brief introduction to these topics is given as they relate to the subsequent.

1.3.1 strength

Strength is typically thought of as the stress at which a structure loses its ability to perform, i.e. bear load, as designed. This concept is easily understood for brittle materials, e.g. ceramics, which typically lose their load bearing capacity catastrophically. In ductile materials, e.g. mild steels, changes in load bearing capacity are usually not obvious to the naked eye and the use of a stress vs. strain curve is often called for. In addition, ductile materials often posses more than one point at which the load bearing behavior changes. These include; proportional limit, where deviation from Hooke's law is noted; yield point, where a significant increase in elongation occurs at an insignificant change in load; ultimate strength, which is the point of highest load bearing and fracture, where all load bearing ceases. The time frame from the proportional limit to fracture can be seconds to years. Typically strength in ductile materials is taken at 0.2% elongation even though this point may not correspond to a change in any material behavior. In polymeric materials load response can be elastic, plastic, viscoelastic or any combination thereof. Typically, these behaviors cannot be distinguished with the naked eye or even with a stress vs. strain diagram. The fact that these materials can undergo elongation of hundreds of percent makes the standardization of strength nearly impossible. Yet defining strength must be done for any material that is to be used in engineering applications.

For composite materials combinations of one or more of the aforementioned materials are involved which means that one is no longer dealing with a simple monolithic material. Load bearing behavior of the composite may be as simple as the load bearing behavior of one of the constituent materials or the composite may behave in a unique manner. For example, in ceramic-ceramic composites, which consist of two brittle materials, the first decrease in load bearing capacity may not be catastrophic. Conversely, in polymer matrix composites reinforced with glass fibers, the onset of deformation in the matrix may not correspond to a decrease in load bearing ability.

In addition, the damage processes which occur in a composite are complicated and typically vary from system to system and even geometry to geometry. The combination of more than one material necessitates the consideration of failure for each constituent. Furthermore, a composite necessarily possesses some interfacial area where shear stresses are introduced. Therefore, simply knowing the tensile strength of the weakest constituent may not be sufficient in determining the strength of the composite. Although shear strength and fiber strength are important for complete understanding of composite behavior, crack growth in the matrix is often assumed to be the phenomenon which defines composite strength in both experimental and numerical work (Aveston et al., 1971; Budiansky et al., 1986, Rubenstein, 1993).

Through-out this work, 'strength' corresponds to the maximum stress sustained by the specimen. For most specimens this strength corresponded to dynamic failure, however, in a particular system, a complicated failure mode resulted in a decrease in load before dynamic failure. Nevertheless, it was the ultimate strength of these specimens that was analyzed. A change in compliance well before the ultimate strength was reached was also observed in some

4

specimens. The stress at which this change in loading response occurred was termed the 'critical stress.'

For specimens with a monolayer fiber architecture a simple uniaxial tension geometry was used. For these specimens ultimate strength was calculated in the typical manner of '...dividing the maximum load on the specimen by the initial cross-sectional area (Timoshenko, 1956).' However, in the case of specimens with multilayer fiber architecture, a compact tension geometry was used. For this geometry calculation of stress, hence strength, is not so straight forward. Due to the compact tension geometry the stress distribution is not uniform and uniaxial. The specimen not only sees uniaxial tensile stresses but also undergoes bending over the ligament. A nominal stress, σ_n, (per unit thickness) at the crack tip of a compact tension specimen can be defined as (Tada, et.,al. 1973)

$$\sigma_n = \sigma_{tension} + \sigma_{bending} = \frac{P}{(w-a)} + \frac{6P\left(a + \frac{(w-a)}{2}\right)}{(w-a)^2} = \frac{P}{(w-a)}\left(4 + \frac{6a}{(w-a)^2}\right), \quad (1.1)$$

where
P = load,
w = specimen width
a = crack length

This equation takes into account stresses due to both tension and bending and assumes the axis of rotation of the ligament is located at the midpoint of the ligament. The 'strength' for compact tension specimens can then be calculated using the maximum load in equation (1.1).

2 EXPERIMENTAL METHODS

2.1 Materials and Properties

2.1.1 matrix material

One matrix material, a three part thermoset epoxy (Dow Chemical Corp.), was used for every composite system of this study. The matrix was prepared from three liquid epoxy precursors; a 'hard' epoxy resin (D.E.R. 383), a 'soft' epoxy resin (D.E.R. 732) and an epoxy curing agent (D.E.H. 24). One unit of the epoxy mixture contained the three precursors in measures of 35.2, 14 and 9.8 g, respectively. The unit mixture was mixed manually by a stirring rod. The mixture was stirred slowly, to reduce the amount of bubble formation, for approximately 5 minutes until the liquid became clear. Depending on the specimen mold, monolayer or multilayer, one to three units, respectively, of mixture were required. The mixture cured at room temperature conditions, 22°C and 50-75% relative humidity, for a minimum of 15 hours. The as-cured mixture, referred to as the 'matrix', was transparent with negligible void formation and shrinkage under ideal conditions. However, curing of the epoxy was highly exothermic. It was observed that if too many units were used to prepare the specimen, the matrix was a deep amber color with severe void formation and shrinkage. Specimens which cured in this manner were discarded.

Matrix strength and strain to failure data were measured from smooth uniaxial tension specimens loaded under displacement control at a cross-head speed, or 'ramp-rate', or 1 mm/min. A typical stress-strain curve for the matrix is shown in Figure 2.1. A linear stress-strain relationship was observed until 2% strain where the behavior became non-linear. An ultimate strength of approximately 50 MPa was reached at which point unloading, in the range 5 MPa, was observed. Fracture occurred randomly within the gauge section and was catastrophic

with little or no fragmentation of the specimen. Table 2-I gives pertinent data for each specimen.

Table 2-I   Experimental data for uniaxial tension specimens.

Specimen	Ramp Rate	Young's modulus	Strength	Load @ 2% Strain	Strain to Failure
Tmat3	1 mm/min	2.2 GPa	48 MPa	2.0 kN	3.4
Tmat4	1	2.2 GPa	50	2.0	4.2

All polymeric materials posses certain viscoelastic properties of which non-linear stress-strain behavior is an indication. These properties may not be revealed under all test conditions, e.g. conditions which induce brittle failure. Non-linear behavior can also indicate material yield. Therefore, the exact source of the non-linear behavior of this material was unknown. Post failure inspection of the specimen under polarized light revealed the presence of localized shear deformation. This observation indicated that yielding of the epoxy had occurred and was most likely the source of unloading. However, the distinction between viscoelastic behavior and yielding in the non-linear region before the ultimate strength was reached was undetermined.

Fracture toughness measurements for the matrix were made from ASTM Standard 399 E compact tension specimens with a characteristic length, w, of 36 mm and a width, B, of 8 mm. Figure 2.2 shows the load-displacement behavior for four specimens. The linear load-displacement and brittle fracture behavior of all specimens indicated that the plain strain conditions required by the standard had been met. Using the fracture load of the specimens in equation (1.1), a nominal strength of 33.7 $\pm$ 1.0 MPa was calculated. From this nominal strength a fracture toughness of 3.3 $\pm$ 0.1 MPa$\sqrt{\text{m}}$ was obtained, Table 2-II.

Table 2-II   Experimental data for matrix compact tension specimens.

Specimen	Characteristic Length and Width, w, B	Crack Length, a	Fracture Toughness, K_{Ic}	Strength, σ_c	Fracture Load, P_c
matrix-1	36 and 8 mm	16.5 mm	3.3 MPa$\sqrt{m}$	34.3 MPa	660 N
matrix-2		16.5	3.1	32.5	628
matrix-3		16.4	3.4	34.8	682
matrix-4		16.6	3.2	33.3	639
Mean		16.5	3.3	33.7	652
Std. Dev.		0.1	0.1	1.0	24

Notice that the nominal strength for the compact tension specimens was over 15 MPa lower than that for the uniaxial tension specimens.

2.1.2   reinforcing material

The reinforcing material was monofilament glass fibers. These fibers, used in the fiber optics industry, consisted of a fused silica core, fluoride doped silica cladding and a polyamide jacket with a total diameter of 0.465 mm, Figure 2.3. Characteristic of the materials used in this work was the fact that, the interface was relatively weak as compared to other systems used in our laboratory (Botsis, et., al., 1995, Beldica, 1996)

Important fiber data are given in Table 2-III. On the same table relevant data of glass and kevlar fibers, used in similar studies in our laboratory, are shown for comparison.

Table 2-III   Relevant data for three reinforcing materials.

Fiber	Manufacturer	Diameter, D_f	Modulus, E_f	Strength, σ_f	Strain to failure, ε_f
Kevlar 29 (Akzo)	Goodfellow	˜ 0.350 mm	58 (100)	n/a	3.7 (2.6)
E-glass	Mexico	˜ 0.350	72.5	2100	2
AnhydroGuide G Monofilament Glass	FiberGuide Industries	0.465	66	˜ 1.5	5-10

2.2   Specimen Preparation

2.2.1 monolayer specimens

Figure 2.4 shows the uniaxial tension mold (with modifications) used in previous studies by this research group. The mold consists of two mold halves and a base. The first mold half is anchored to the base while the second mold half is attached to the first via a screw and nut located in each corner. This mold allowed rectangular tension specimens to be uniaxially reinforced with a single row, or 'monolayer', of well aligned fibers at virtually any fiber spacing.

The mold consisted of machining grooves in each half of the mold ends to allow simple and accurate alignment of the fibers and also to allow the mold halves to come together flush to prevent leakage. Grooves 0.25 mm deep, 0.5 mm wide and 0.75 mm center-to-center were machined into each half of the mold ends. This allowed the 0.465 mm diameter fibers to be well aligned and held firmly in place in center-to-center increments of 0.75 mm.

Before fiber alignment both mold halves were freed of any residual cured epoxy or mold release from previous sample preparations. Then the mold halves were wiped with methanol and a clean cloth and sprayed with Epoxy Mold Release (Crown 353).   The alignment method was straightforward. With the mold halves separated, the mold base and anchored half were laid horizontal. Fibers approximately 5 cm longer than the mold were placed in the machined grooves at the desired fiber spacing. The free half of the mold was then joined to the anchored half, still in the horizontal position. Matching grooves on both halves allowed the halves to be tightened flush via the corner screws without crushing the glass fibers.

A suitable method for clamping the fiber ends (recall that fibers were longer than the mold) was needed. Rubber gasket strips, 2.8 mm thick, were glued to both sides of the contact point of a 2.5 cm capacity paper binding clip, one clip for each end of the mold. The clips were placed on the fiber ends in such a manner that the rubber gasket strips firmly gripped the fibers. One clip was then anchored while a dead load of approximately 2.5 N was applied to the other clip. The dead load resulted in an average pre-stress of 2 MPa on the fibers. This stress was neglected in subsequent analysis. Bending of the fibers was observed if the mold halves were over tightened, if the anchored clip, mold and dead weight were not collinear and/or if the clips were allowed to rotate. Precautions were taken to avoid these situations.

To address the problem of leakage, silicone gel (General Electric), was used on all mold joints. Due to the alignment set-up, the gel had to be applied to the ends of the mold, i.e. on the grooves, before the fibers were gripped. Even though the gel was allowed to cure for at least an hour before the epoxy was poured into the mold, it began to set in only 15 minutes. Therefore, fiber 'straightening' had to be performed as soon as possible after the gel was applied to prevent breakage of the gel-mold seal near the grooves when tension was applied to the fibers. A subtle point about the use of the silicone gel was that it was found to be an excellent way of keeping the joining screw threads from becoming covered with epoxy that inevitably leaked from the inside of the mold.

7

A small amount of gel was applied to the screws before they were screwed into the mold halves. The flexible nature of the as-cured gel offered no resistance to screw removal but at the same time prevented contact of the epoxy with the screw during epoxy curing.

After the required epoxy cure time, the tension set-up was removed, the mold halves separated and the as-cured composite 'bar' was removed. The as-cured bar had a total length of 196 mm, grip lengths of 25 mm, and a width of approximately 26 mm. The grip thickness was approximately 8 mm and the gauge thickness 2.3 mm. Each as-cured bar was machined into one of two uniaxial tension test geometries, dog-bone or notched, with the gauge width of as-machined specimens determined by the formula $W = n\lambda + 3$; where n was the number of fibers and λ was the fiber spacing and 1.5 mm was allowed from the end fibers to the specimen edge. Figure 2.5 shows the dimensions of both the dog-bone and notched tensile specimens, note that only the width of the specimen was machined, the length as thickness remained at the as-cured dimensions. A machined notched, with an angle of 60°, was introduced into one side the 'notched' specimen such that the crack tip was approximately 0.5 mm from the 'leading' fiber. The machined surfaces, as well as angled section of the specimen between the grip and gauge section, were smoothed manually using water and 60 grit paper.

2.2.2 multilayer specimens

For the multilayer fiber architecture an entirely new mold had to be designed to build a fiber architecture with the monofilament glass fibers.

The key to this new mold was the method by which the fibers were held in place and tightened. It should be stated here that the mold was completely disassembled and cleaned in the usual manner before each specimen preparation. This was absolutely critical with this mold to assure fluid movement and flush joining of all parts. The mold consisted of a skeleton with two end pieces, one of which was anchored to the base and the other which was movable along four guiding rods by means of a screw mechanism. Each end piece consisted of a frame-screen-frame sandwich, Figures 2.6 and 2.7. The brass screen (McMaster-Carr) had 0.5 mm diameter holes spaced 0.75 mm apart center-to-center in a square grid pattern. Two sections of the screen were precisely cut to identical dimensions. Four large holes were drilled in the screen, one at each corner, which matched screw holes drilled into frames. The screen was then placed between the frames and the sandwich secured with a nut and bolt combination in each corner.

Again the dimensions of the desired compact tension specimens had to be calculated prior to fiber alignment. The first fiber was slipped through the appropriate hole in the screen, across the length of the mold and through the matching hole of the other screen. Because the fiber diameter was 0.465 mm and the screen hole diameter was 0.5 mm, the fibers were snug in the holes and fiber shifting was impossible. In theory, the fiber alignment should be as 'perfect' as the screen hole alignment. This process was repeated at the desired x- and y-direction fiber spacing until the fiber architecture was complete. Note that the fibers were cut approximately 30 mm longer that the desired length of the bar at each end.

Next, silicone gel was used to entirely seal both screens. The extra fiber lengths at each end of the mold were completely encased in a massive blob of gel. This step was critical because as the fiber spacing became smaller the capillary action of the gel between fibers tended to pull the fiber ends together causing additional curvature of the fibers across the length of the mold. At a 0.75 mm x-direction fiber spacing, the surface-to-surface fiber distance was only 0.25 mm. At such a fine fiber spacing, the force of the curing gel, as well as the curing epoxy, lead to unavoidable variations in fiber alignment. Once the gel had been applied it was allowed to cure for a minimum of 6 hours, due to the thickness of the gel blob on the ends of the fibers.

After the gel cured, the mobile end of the mold was moved away from the anchored end. The gel blobs held firmly onto the fiber ends during movement of the frame, hence stretching the

fibers straight. Once the mold ends were in the correct position, a bottom plate was slid underneath the bottom two guiding rods and two side plates were slid inside the side guiding rods. (Note that the lengths of the plates had been calculated *a priori* so that they slid into place leaving virtually no gaps.) Each side plate was joined to the base plate, as well as the frames, to form a trough around the fibers. The joints were then sealed with silicone gel which was allowed to cure for approximately one-half hour. The liquid epoxy was then poured into the trough and allowed to cure for the requisite 15 hours. After curing the mold was disassembled and the composite bar was removed. Compact tension specimens were cut from such bars with dimensions according to ASTM standards for fracture toughness, Figure 2.8.

In all CT specimens, the machined 'crack' was brought to within 1.5 mm of the first fiber row then a razor blade was used to introduce a sharp crack tip to within approximately 0.5 mm of the first fiber row.

The beauty of this mold was in the versatility of the fiber architecture which could be built. By replacing the screens, not only could many fiber diameters be used but the grid pattern of the fiber architecture could be customized. The possibilities are only limited by the screen geometry, of which there are many.

2.3 Mechanical Testing

An Instron 8500 hydraulic mechanical testing unit was used for the mechanical testing of all specimens. A PC with Instron Series IX software was used to collect load-displacement data. One compact tension specimen series was loaded using a loading-unloading, or dual-ramp, waveform. This testing consisted of loading the specimen to a prescribed actuator displacement then unloading the specimen to the initial displacement. The ramp-rate for both loading and unloading was constant.

The loading loop was repeated, in increments of 0.5 mm, until the specimen fracture. Between each loop a downtime of approximately 1 to 2 minutes was required while the parameters for the next loading loop were set.

The grip fixtures for the uniaxial tension specimens were identical for the top and bottom grips. Both were self-aligning grips in the plane parallel to the loading direction but perpendicular to the width direction of the specimen. For the CT specimens, pin loading fixtures were used.

For the uniaxial tension specimens, no preload was applied. This resulted in a small region of an apparent increase in displacement under no load on the load-displacement curves. This was due to alignment of the grips and this region was removed from the analyzed data. For the CT specimens, rotation about the loading pins was removed manually by applying a small preload.

2.4 In-Situ Observation

The uniaxial tensile specimens were observed unaided during loading as well as with the aid of polarizers. Using a bright, but diffuse white light source and two polarizing plates, one behind the specimen and one in front, the stress patterns of the specimens were observed. No attempt was made to quantify the observations using the polarizers.

Observations of the CT specimens tested with a single-ramp waveform were made only at the crack tip using an optical microscope, specially mounted for use horizontally. An image at 80X magnification was piped through a CCD camera where the image was viewed on a monitor. The microscope traveled along all three axes in order to follow crack growth or other fracture processes. The *in-situ* loading response was recorded using standard VHS format video tapes at normal recording speeds.

2.5 Acoustic Emission

Acoustic emission is the term applied to a stress wave, in the acoustic range, which is released from damage phenomenon occurring in a specimen under loading. The method of acoustic emission is an active, but 'contact', method which involves joining sensors, with the proper acoustic properties based on the expected stress waveforms, to the specimen surface which record the released stress waves. A discussion of wave mechanics is beyond the scope of this paper. However, a few basic concepts of acoustic emission will be discussed to aid in the understanding of the methods employed in this work.

First, the interface between a surface and the ambient atmosphere is a strong wave scatterer, therefore acoustic sensors require a coupling medium through which the stress waves can propagate relatively unimpeded. This medium may be as simple as a grease, with the sensor held in place by tape, or as complicated as a water medium which is contained by special attachments. The sensors can also be soldered to the surface if the application warrants and if the sensors are tolerant to this treatment. The important point about sensor coupling is that the medium should be distributed evenly across the sensor and no inclusions, which will scatter the stress wave, are present.

Second is the fact that the acoustic emission equipment cannot record all stress wave which bombard the sensor. Beginning with the sensor, through the wave conditioner and into the data acquisition hardware, the system electronics are sensitive to the wave properties, especially the frequency, and rate of data flow. In addition, even in the case where the electronic set-up can capture a wide range of waveforms, the user must set certain parameters based on the type of stress waves of interest to the researcher. An example various waveform parameters that must be set by the user, e.g. peak definition time, PDT, hit definition time, HDT, and hit lock-out time, HLT, are shown in Figure 2.9.

When a stress wave makes contact with the sensor it is called a 'hit'. For each hit one can measure the amplitude, duration and energy, as well as the hit rate. In addition to information on a hit, the location of the wave source can be found in two or three dimensions.

Even though a wealth of information is available from this method, is common to concentrate only on a few aspects of the recorded data. The energy of a hit may be the most descriptive an informative piece of data one can get from a damage process. Yet, it is often the hardest to measure and calibrate.

In composite research were the damage processes are many and varied, the quantitative values of hits, e.g. amplitude, duration and energy, are generally not indicative of particular damage mechanisms (Daniel, 1993). At any rate, it is commonly reported that matrix damage such as plastic deformation and shear-band formation, are sources of low acoustic energy while fiber-matrix separation, debonding and delamination are sources of medium acoustic energy and fiber and matrix fracture are sources of high acoustic energy. Yet, without specifically calibrating the acoustic emission behavior of each constituent material separately, as well as in composite form, one cannot make such general statements as to the source of acoustic activity. Also, these signals often overlap making it difficult to separate the data on the basis of amplitude, energy etc.

With all this information available, yet difficult to interpret, it is no wonder that it has become common practice to report the easiest to measure and simplest to understand data available. Rate of acoustic activity and the cumulative number of hits is often the data reported, with these two quantities being qualitatively related to damage intensity and total damage, respectively. The data is then correlated to visual observations or mechanical data in a way that a 'critical' value for some condition, e.g. load, has been met or exceeded. The investigation that follows is no exception. Based on some simple acoustic emission data, visual observations were better understood and a complete picture of the composite behavior was then drawn.

10

A Physical Acoustics Corp. (PAC) Spartan 2000 and PAC SA-DAQ software were used to record acoustic emissions from in-situ testing of dog-bone and compact tension specimens. In both cases, two 6 mm diameter PAC S9220 sensors, connected to PAC 1220A preamplifiers with 40 dB gain, were attached to the specimens, Figure 2.10, with silicone gel as the couplant. The specimens laid flat and manual pressure was applied to the sensors while the gel was allowed to set. Upon setting the gel formed an adhesive bond between the sensor and specimen. Acoustic emission recording parameters were set at 40 dB threshold and Peak Definition, Hit Definition and Hit Lock-Out Times of 50, 200 and 300 ms, respectively. These values were based on data supplied in manufacturer literature for testing of composite materials.

2.6   Post-Failure Analysis

Three optical methods were used to conducted post-failure analysis of all specimens. First, a stereoscope was used between 0.8 and 6.4X magnification. Viewing the specimen with this piece of equipment allowed the observation of fracture behavior on a macroscale. Subtle surface textures and curves are visible that cannot be seen by the naked eye. Behavior that changed slowly or over a large area can easily be detected, as well as the change in behavior in relation to other specimens features.

An optical microscope was used in the magnification ranges between 40 and 80X to make accurate measurements of microstructural features. These features included fiber radius, fiber spacing, sharp crack tip length, i.e. the crack introduced by a razor cut, and zones of different behaviors. Again, this equipment allowed one to see features that were difficult with other methods. For example, the initial steady-state crack growth region and the change to dynamic crack growth were very sharp at this magnification.

Finally, scanning electron microscopy, SEM, was an invaluable tool for observing highly localized effects and fine structures. Through the use of this method information on bonding surfaces and interfaces can be gathered. Indeed, it will be shown that through the use of SEM, the origin of composite failure was located and the hypothesis about the type of interface present was validated.
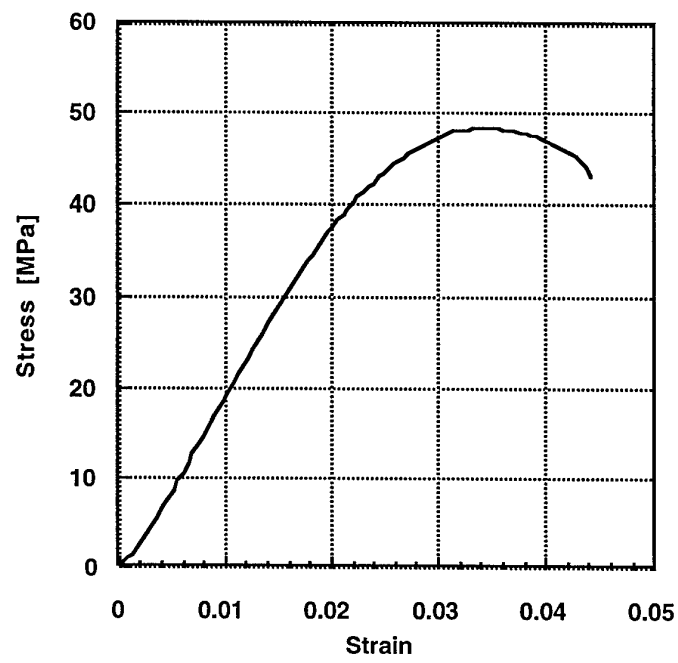
Figure 2.1   Stress vs. strain for smooth uniaxial matrix specimens.
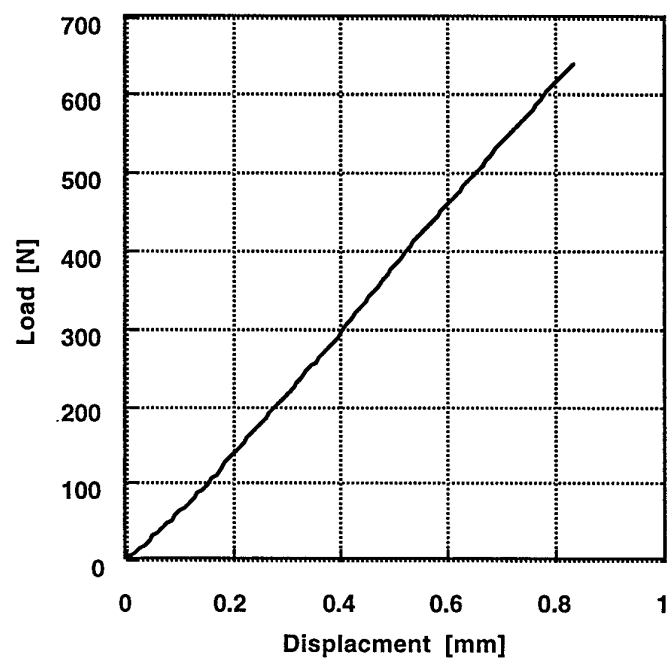
Figure 2.2   Load vs. Displacement for Matrix Compact Tension Specimens.

silica core

Fluoride doped silica 'cladding'

Polyamide 'thermo-coat'

400 μm

440 μm

465 μm
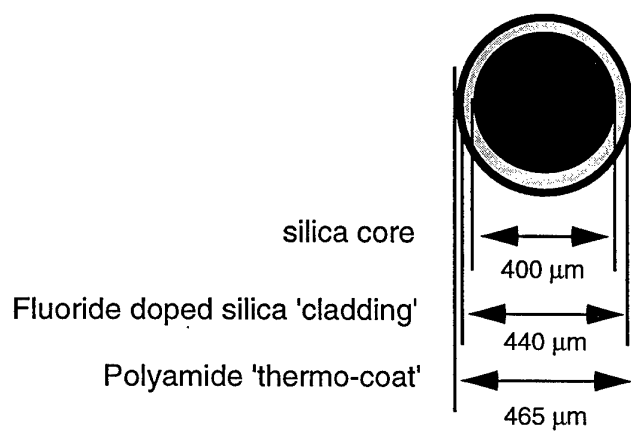
Figure 2.3　　　Schematic of monofilament glass fiber cross-section.

0.5 mm

0.25 mm

0.25 mm
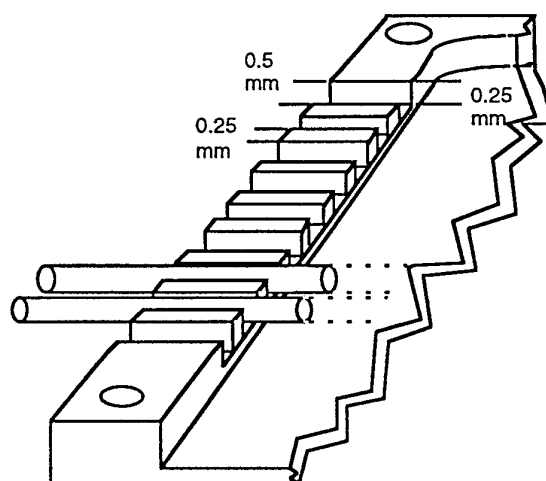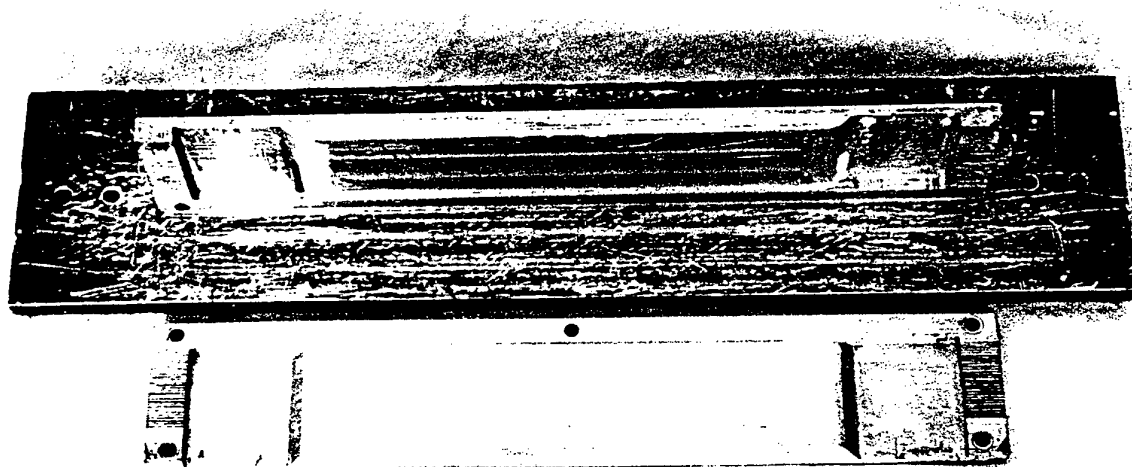
Figure 2.4   Modified monolayer fiber architecture fabrication mold.

15

Figure 2.5   Schematic of dog-bone and notched uniaxial tension specimens.
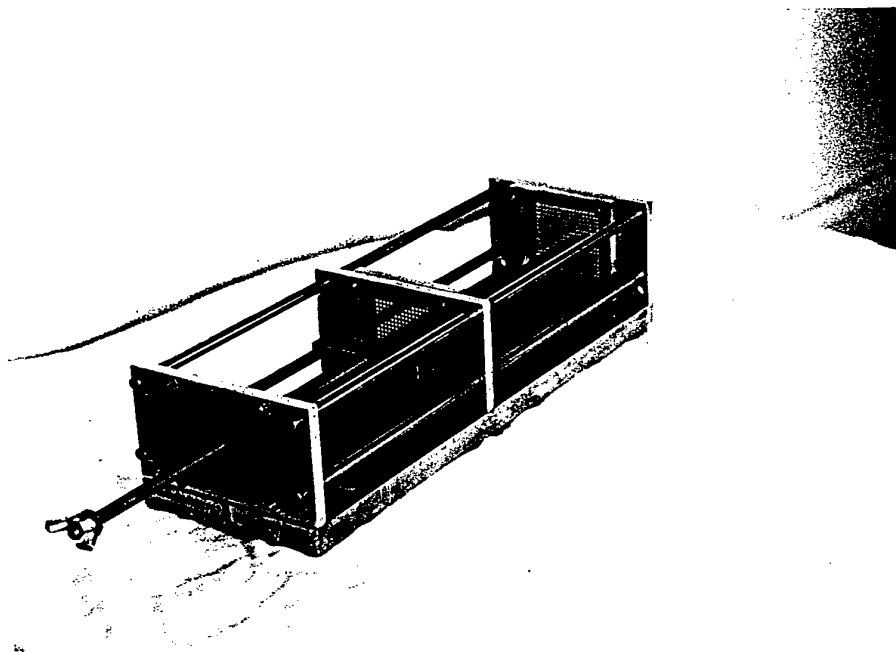
Figure 2.6   Compact tension mold for use with rigid monofilament fibers.
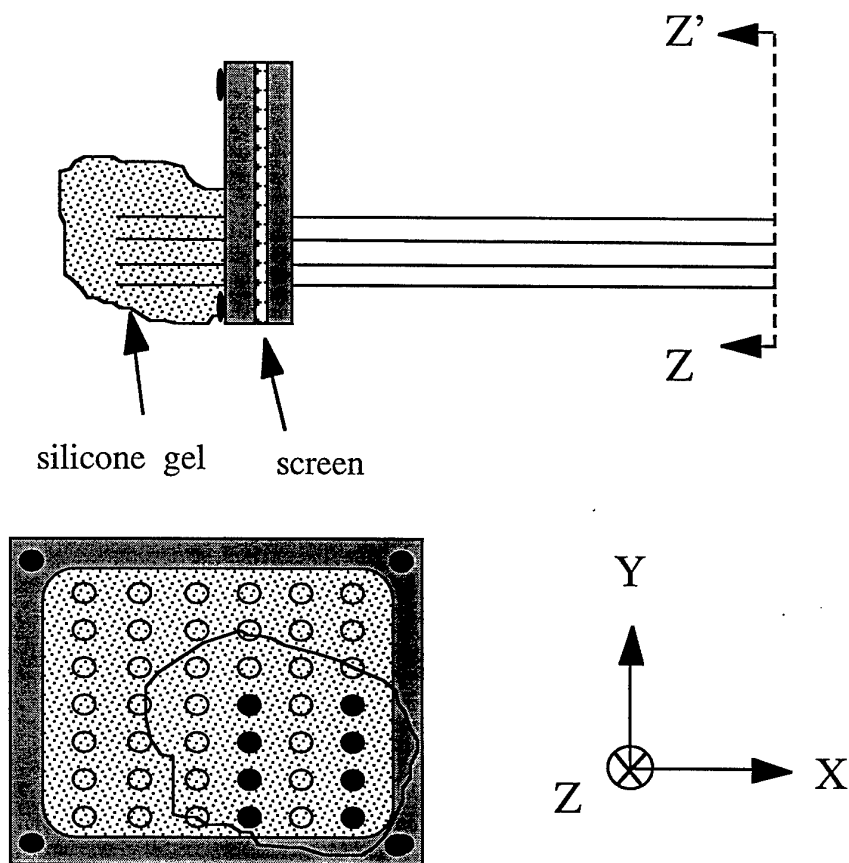
Figure 2.7   Schematic of rigid mold ends and fiber alignment methods.
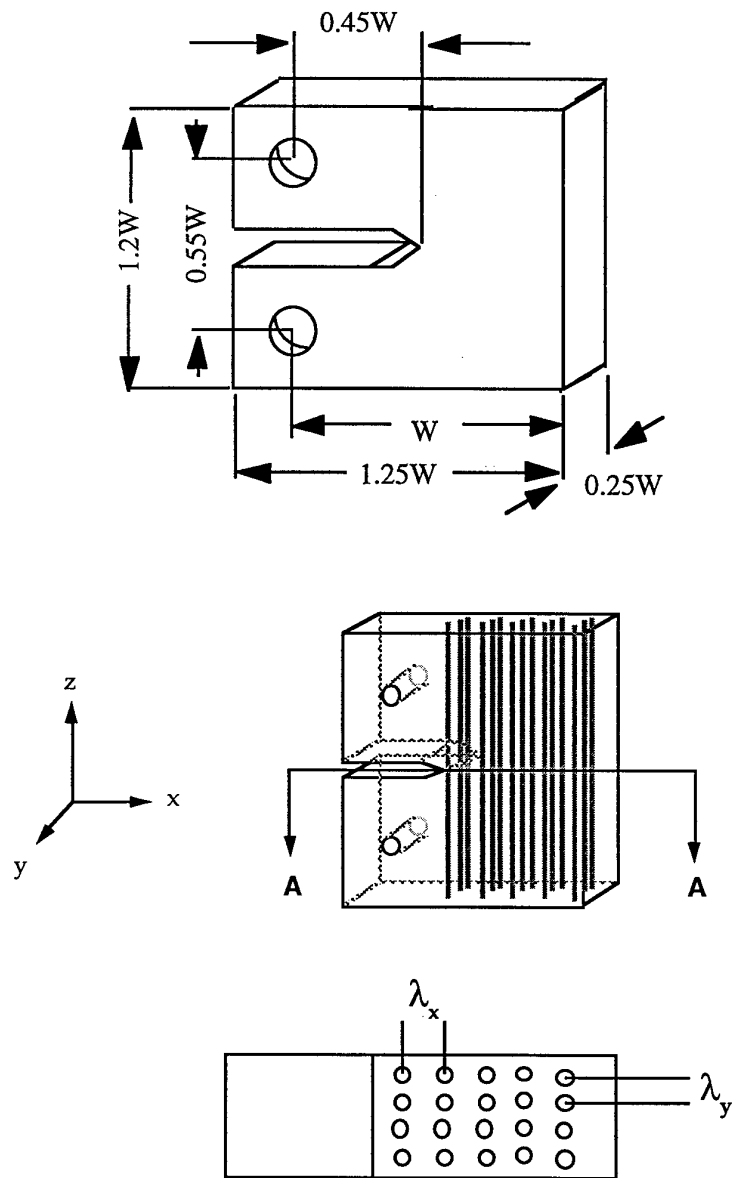
Figure 2.8   ASTM Standard 399 compact tension specimen geometry and reinforced specimen.
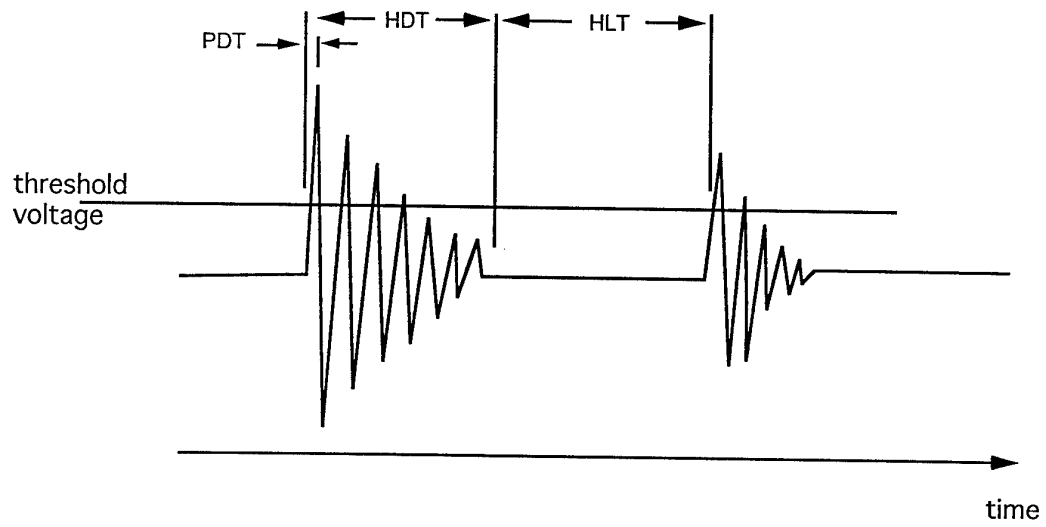
Figure 2.9   Schematic of an acoustic waveform and various parameters.
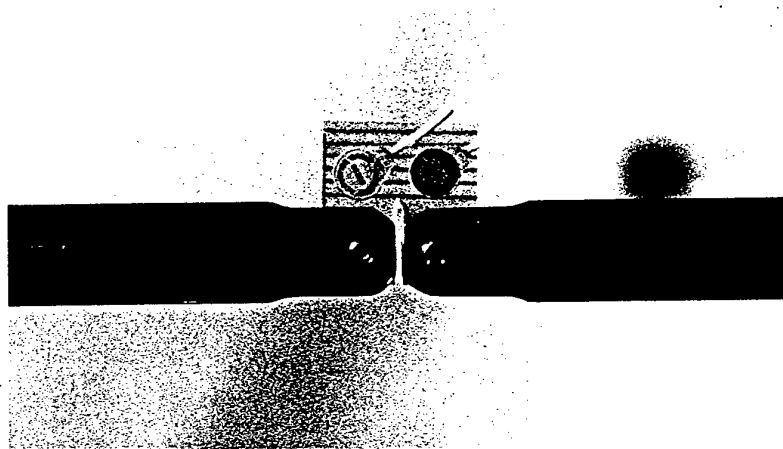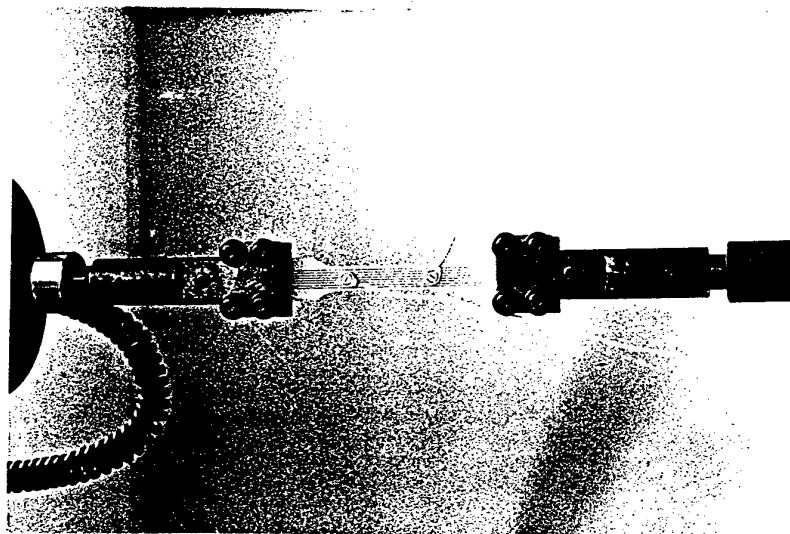
Figure 2.10   Location of acoustic emission sensors for both dog-bone and compact tension specimens.

3 MONOLAYER FIBER ARCHITECTURE

3.1 Introduction

In this chapter the mechanical properties and fracture behavior of a model composite system with a monolayer fiber architecture are reported. Fiber spacing, λ, of 0.75, 1.5 and 2.25 mm were used in the reinforcement of the notched specimens while fiber spacing of 1.5 and 2.25 mm were used in the dog-bone specimens.

The mechanical behavior of the specimens, i.e. the stress-strain curves, were investigated through visual observation and acoustic emission methods. It was found that the elastic response of the specimens, as well as the on-set of non-linear stress-strain behavior (referred to as the proportional limit) and the ultimate strength of the specimens, could be described as a function of the fiber spacing.

Properties of the fiber-matrix interface were obtained from a dog-bone tensile specimen in which a matrix through crack occurred at a stress much lower than the strength of the fibers, hence allowing the fibers to remain intact across the matrix crack, simulating a fiber pull-out test.

Post-failure analysis of the fracture surfaces showed that matrix fracture, which corresponded to composite failure, initiated in every case at the fiber-matrix interface.

3.2 Experimental Observations

Experimental stress-strain curves for uniaxial loading of the unreinforced matrix and the two composite geometries are shown in Figure 3.1 and Figure 3.2, respectively. The matrix material initially displayed a linear elastic behavior with a Young's modulus of 2.2 GPa. At approximately 2% strain the behavior of the matrix became non-linear with fracture occurring near 3.7% strain. The addition of reinforcing fibers increased the stiffness of the specimens. As the fiber spacing decreased, i.e. the number fibers increased, the material not only became stiffer but the range of linear elastic behavior also increased. Even at a low fiber volume fraction of 7.3%, linear elasticity almost completely dominated the composite behavior. Each of the composite specimens displayed a similar strain to failure, approximately 4.3%. This showed that the presence of the fibers modified the strain behavior of the matrix. However, the strain to failure of the composite specimens appeared to be independent of fiber spacing.

The experimental stiffness of the composite specimens was compared to the stiffness predicted by the ROM, i.e.

$$E_{rom} = E_m V_m + E_f V_f,$$ (3.1)

where
E_m and E_f = Young's modulus of the matrix and fiber, respectively, and
V_m and V_f = volume fraction of the matrix and fiber, respectively.

Excellent agreement was observed between the experimental and theoretical responses, Table 3-I. It was interesting to note that the presence of the notch had virtually no effect on the composite behavior. This was explained by the fact that bulk properties, such as Young's modulus, are typically not affected by a single flaw which is small, say less that 10%, compared to the dimensions of the specimen. Debonding of the first and second fibers directly ahead of the notch tip was observed. This indicated the presence of the Gordon mechanism (Cook and Gordon, 1964), whereby the increased stresses at the crack tip induce separation of the fiber from the matrix which in turn absorbed enough energy to arrest crack growth. This mechanism also helped the notched specimens retain a strength identical to the unnotched specimens.

The most interesting feature of the composite behavior was the onset of non-linear stress-strain behavior and the changes of this behavior as a function of fiber spacing. To investigate the processes controlling this behavior, acoustic emission methods were coupled with uniaxial testing. Figure 3.3 shows the number of hits, and the associated energies, superimposed on the load-displacement curve for a typical dog-bone specimen. Notice that acoustic activity began at the proportional limit of the stress-strain behavior. Both the number of hits and energy were observed to increase with loading. Qualitatively it appeared that the energy remained proportional to the hits up to fracture suggesting that only one damage process was occurring. However, at fracture the energy greatly increased while the number of hits decreased.

Table 3-I.   Testing conditions and results for uniaxial loaded monolayer model composite geometries.

Specimen	Ramp Rate	Fiber Spacing, λ	Volume Fraction, V_f	Young's mod. experimental, E_{exp}	Young's modulus ROM, E_{rom}	Strength, σ_c
TGMB -1	30 mm/min.	0.75 mm	7.3 %	5.8 GPa	6.8 GPa	248 MPa
TGMB -2	30	0.75	7.3			249
TGMA -3	30	1.50	3.8	4.2	4.6	153
TGMA -4	30	1.50	3.8			160
TGMA -5	30	1.50	3.8			177
TGMC -1	30	2.25	2.5	3.7	3.7	119
TGMC -2	30	2.25	2.5			122
91MB -a	1	1.50	4.1	4.6	4.8	164
91MB -b	1	1.50	4.1			149
91MB -c	1	1.50	4.1			172
91MC -a	1	2.25	2.5	3.7	3.7	119
91MC -b	1	2.25	2.5			120
91MC -c	1	2.25	2.5			109

It is commonly reported that matrix damage such as plastic deformation, shear-band formation, are sources of low acoustic energy while fiber-matrix separation, debonding, delamination and friction are sources of medium acoustic energy and fiber and matrix fracture are sources of high acoustic energy. Yet, without specifically calibrating the acoustic emission behavior of each constituent material separately as well as in composite form, one cannot make such general statements as to the source of acoustic activity. Although calibration of this system was not performed, based on the observation of fiber and matrix fracture only at composite failure, it was concluded that damage at the fiber matrix interface was the source of stress-strain non-linearity.

3.3 Role of Fiber Spacing

Based on the preceding discussion an attempt was made to correlate proportional limit, or on-set of non-linearity, with fiber spacing. A simple yet powerful method for this type of investigation is dimensional analysis (Barenblatt, 1987). The first step in this analysis was to list all the parameters on which the proportional limit, or critical stress for the fiber-matrix interface, σ_c^i, was believed to depend on;

$$\sigma_c^i = \Phi_0\left(K_c^i, \lambda, E_m, E_f, D_f, w, b, l,\right),$$ (3.2)

where

23

K_c^i = fracture toughness of the fiber-matrix interface,

λ = fiber spacing,

E_m, E_f = Young's modulus of the matrix and fiber, respectively,

D_f = fiber diameter and

w, b, l = specimen width, thickness and length.

If fiber spacing and interface fracture toughness are taken as the fundamental parameters, equation (3.2) can be rewritten as

$$\sigma_c^i = \frac{K_c^i}{\sqrt{\lambda}}\Phi_1\left(\frac{E_m\sqrt{\lambda}}{K_c^i}, \frac{E_f\sqrt{\lambda}}{K_c^i}, \frac{D_f}{\lambda}, \frac{w}{\lambda}, \frac{b}{\lambda}, \frac{l}{\lambda}\right) \qquad (3.3)$$

where

$$\Pi_1 = \frac{E_m\sqrt{\lambda}}{K_c^i}; \; \Pi_2 = \frac{E_f\sqrt{\lambda}}{K_c^i}; \; \Pi_3 = \frac{D_f}{\lambda}; \; \Pi_4 = \frac{w}{\lambda}; \; \Pi_5 = \frac{b}{\lambda}; \; \Pi_6 = \frac{l}{\lambda}.$$

Note that in equation (3.3), once the fundamental parameters are chosen they must be combined in such a way that their product is dimensionally equal to the governed parameter. Now, according to dimensional analysis theory, any of the dimensionless 'pi' terms can be eliminated if they are much greater or much less than unity, provided they are not unbounded. Therefore, since $\Pi_1 \approx 10^2$, $\Pi_2 \approx 10^3$ and $\Pi_5' = \Pi_6 / \Pi_5 \approx (100 \div 2)$, these terms may be neglected. The remaining pi terms may be combined in any fashion for simplicity and convenience of expression. The final expression is

$$\sigma_c^i = \frac{K_c^i}{\sqrt{\lambda}}\Phi_2\left(\frac{D_f}{w}\right). \qquad (3.4)$$

The only criteria necessary to validate the previous assumptions, and the form of equation (3.4), is that the experimental data fits the model. Although the exact form of Φ_2 was not known, because the fiber diameter, specimen width and interface fracture toughness were constant, or assumed constant in the case of the interface fracture toughness, these terms were combined into a single constant, κ. The equation,

$$\sigma_c^i = \frac{\kappa}{\sqrt{\lambda}}, \qquad (3.5)$$

was applied to the proportional limits for each composite specimen. From Figure 3.4 it can be seen that the correlation between the experimental data for onset of non-linearity in the composites did indeed fit the proposed model, equation (3.5).

The proposed model was also correlated to the composite fracture stress, also in Figure 3.4. When the linear relationship was forced through the origin, an increasing deviation from the linearity with increasing fiber spacing was observed.

To investigate the deviation of the fracture stress from the model, the linear region of each stress-strain curve was extrapolated to the failure strain of the composite, approximately 4.3% in every case. This 'extrapolated' fracture stress was then compared to the model. Indeed, this 'extrapolated' fracture stress, also in Figure 3.4, showed the same trend as the proportional limit, i.e. a linear relationship that extended through the origin. The higher 'extrapolated'

24

fracture stresses for the dog-bone specimens were due to the slightly higher stiffness of these specimens.

Following the success of describing the proportional limit and fracture stress with the model proposed in equation (3.5), the influence of fiber spacing over the entire range of stress-strain behavior was investigated. Again, starting with the root of fiber spacing as a critical parameter, it was found that the linear region of the stress-strain behavior scaled with the factor $\sqrt{\lambda}/\sqrt{w}$ for both the specimen geometries, Figure 3.5 and Figure 3.6. Note that the width of the specimens was constant for each geometry and was used simply to make the scaling parameter dimensionless. Again these scaled stress-strain curves deviated slightly from one another at the onset of non-linearity reminiscent of the fracture stress deviation from equation (3.5).

3.4 Role of Fiber Volume Fraction

The correlation of the proportional limit, fracture and extrapolated fracture stresses to fiber volume fraction was also investigated. The stresses as a function of fiber volume fraction are shown in Figure 3.7. However, the linear relationship of the stresses as a function of fiber volume fraction did not extend through the origin, but instead a unique intercept for each stress relationship was observed.

The strength predicted from the ROM was then compared to the experimental fracture stress. Recall that the ROM for composite strength, σ_c, for a fiber strain to failure greater than that of the matrix, is

$$\sigma_c = \sigma_m^* V_m + \sigma_f' V_f \qquad (3.6)$$

where

σ_m^* = fracture stress of the matrix,

σ_f' = stress on the fibers at the fracture strain of the matrix and

V_m, V_f = the volume fraction of matrix and fiber, respectively.

The strain to failure of the matrix was taken from experimental values of the pure matrix under uniaxial loading. Then using Hooke's law and the manufactures data for fiber Young's modulus, the stress carried by the fibers at composite failure was calculated, i.e. $\sigma_f' = E_f \varepsilon_c = 66$ GPa * 0.037 = 2.4 GPa. The results from this model as a function of fiber volume fraction and fiber spacing were compared to the experimental fracture stresses. In both cases the strength predicted by the ROM was slightly lower than the experimental fracture stress. As expected from equation (3.6), when the ROM strength was plotted as a function of fiber volume fraction, the intercept was equal to the strength of the matrix.

Although good correlation between the experimental fracture stress and the ROM strength was observed, the difference between the predicted and experimental fracture values, even though small for this composite system, raises two important issues. First is the use of matrix strain to failure for ROM strength calculations. Through reinforcing a material, one typically attempts to increase the strength of that material. However, the increase in strength is often accompanied by a change in the strain to failure properties of the reinforced material. As stated in the introduction, the ROM for strength does not take into consideration any change in matrix (or fiber) properties due to the presence of the fibers (or matrix). The ACK model (Aveston et al., 1971) addressed this issue and presented a model that could be used to predict the changes in fracture strain of the matrix as a function of the fiber volume fraction. An attempt was made to apply this model to the present system but the behavior of the constituents was found to violate the applicability of the ACK model.

25

The second important limitation of the ROM is that it depends on volume dependent properties. While this is valid for transport, i.e. bulk, properties, such as Young's modulus, it is dangerous to apply such a model to a property, e.g. strength, that depends on local morphology. As has been shown for other systems, e.g. glass, concrete, ceramics (Griffith, 1921; Botsis et al., 1995), strength is more accurately modeled using parameters that describe the microstructure of a material, such as flaw, pore or grain size or, as has been demonstrated here, fiber spacing.

3.5 Interface Properties

Damage of the fiber-matrix interface was observed during testing of the notched specimens. In addition, acoustic emissions were recorded at the onset of non-linearity in the dog-bone specimens. Important interface parameters controlling such processes, such as interfacial strength and the work of fiber debonding and sliding (Kerans et al., 1989) can be found from fiber pull-out testing. In this investigation a standardized pull-out test was not performed. However, qualitative fiber and interfacial strength data were obtained from a test specimen in which the matrix fractured at a load sufficiently low to leave the fibers intact across the matrix crack.

In a dog-bone specimen with fiber spacing of 1.5 mm, 8 fibers, the matrix fractured at approximately 38 MPa. The fibers remained intact across the matrix crack until the ultimate stress of the fibers, approximately 1.5 GPa, was reached. Upon reaching this stress seven fibers fractured at the matrix crack but one fiber fractured in the gauge section of the specimen, 35 mm from the matrix crack. Therefore, the specimen simulated a pull-out test with an embedded fiber length of 35 mm. Figure 3.8 shows the complete load-displacement curve for this specimen. Note the matrix fracture at 1400 N, fiber failure at 2100 N and pull-out behavior of the embedded fiber from 3 to 30 mm.

For a system with a purely frictional interface, a simple load balance between tensile stress on the fiber and shear stress at the fiber-matrix interface can give a first approximation to the shear strength of the interface, τ_i, i.e.

$$\tau_i = \frac{\sigma l^*}{2\pi r}$$

(3.7)

where
σ = tensile stress on the fiber,
r = fiber radius and
l^* = embedded fiber length.

Typically only one peak, corresponding to some critical stress, is observed during a pull-out test. This critical stress can indicate the onset of debonding, for chemically bonded fibers, or sliding, for purely frictional interfaces. However, the load-displacement curve from this particular specimen showed two peaks, 469 and 357 N, during loading of the embedded fiber. Although the shape of the two loading curves were typical for fiber pull-out, the presence of two peaks was not. Due to the purely frictional interface the peaks were initially believed to be due to a 'slip and catch' mechanism. However, upon inspection of the specimen it was found that the fiber had fractured three times, at depths (from the matrix crack) of 35 mm, 33 mm and 27 mm.

Although *in-situ* fiber fracture was not observed, the following process was hypothesized. At a load of 2100 N seven fibers fractured at the matrix crack with the eighth fiber fracturing 35 mm deep in the matrix. The embedded fiber was at an exceptionally high strain rate in the instant after fiber fracture. This rate was sufficient to initiate fiber pull-out. A correction in strain rate by the Instron feedback loop, i.e. the displacement loop at 3 mm, allowed frictional forces at the fiber-matrix interface to take hold. Under continued loading of the fiber, at the programmed 1 mm/min. strain rate, the strength of the fiber was reached before the interfacial shear stress could overcome frictional bonding, resulting in fiber fracture instead of fiber pull-out. Due to the large embedded length of the fiber, the tensile stress on the fiber built reached

26

the fiber strength again before friction was overcome and the fiber fractured a second time. Upon failing a second time the embedded fiber length was reduced below the critical value for pull-out and/or the interface had been degraded to such a degree that fiber pull-out ensued.

The embedded fiber lengths at fracture were measured from the two fiber fragments left behind in the matrix. Using these embedded lengths (33 and 27 mm) and the tensile stresses present at the two peaks (2,775 and 2,112 MPa) following initial fiber failure, shear stress values of 9.78 and 9.09 MPa were calculated from equation (3.7).

3.6 Fracture Mechanisms

In every composite specimen catastrophic failure occurred at the peak load. It was observed that composite failure initiated with matrix cracking. In the split seconds after total matrix failure, the fibers momentarily transferred the sudden increase in load thrust upon them to regions of the matrix away from the initial matrix crack inducing secondary matrix cracking and failure of the fiber at random weak spots before 'instantaneous' failure of the fibers across the initial matrix fracture occurred. Fragmentation and secondary matrix cracking was, qualitatively, inversely proportional to the fiber spacing, i.e. lower fiber spacing yielded more damage. Combining *in-situ* observations with acoustic emission and stress-strain data the fracture process shown in Figure 3.9 was hypothesized.

Inspection of the fracture surfaces revealed that the fracture mechanism was identical in all specimens. Figure 3.10 shows a typical fracture surface for the monolayer specimens. A fracture morphology similar to the familiar mirror-mist-hackle morphology was observed. The mirror surface was centered around a single fiber and radiated outward. The mirror surface began to change to a 'mist' surface as it approached neighboring fibers. Far away from the mirror surface a 'hackle' surface (not shown), typical of dynamic fracture in polymers, was observed. This surface morphology pointed to a random defect at the fiber-matrix interface as the nucleation site for matrix, hence composite, failure.

Due to the observation that matrix fracture initiated at the fiber-matrix interface, it can be concluded that the distribution of the fibers was able to reduce the effect of stress concentrators, e.g. machined notches, voids, etc., located in the bulk of the matrix. The fact that strain to failure data of the composite specimens was consistent, yet greater than the unreinforced matrix, suggested that the presence of the fibers was able to modify the strain to failure behavior of the matrix but only to some critical value, 4.3% for this system. The increase in strength for successively decreasing fiber spacing suggested that not only did the fibers exert more of an influence on overall composite properties, e.g. stiffness, but that fiber-fiber interactions became increasingly important helping to reduce the stress concentrations introduced by defects at the fiber-matrix interfaces.
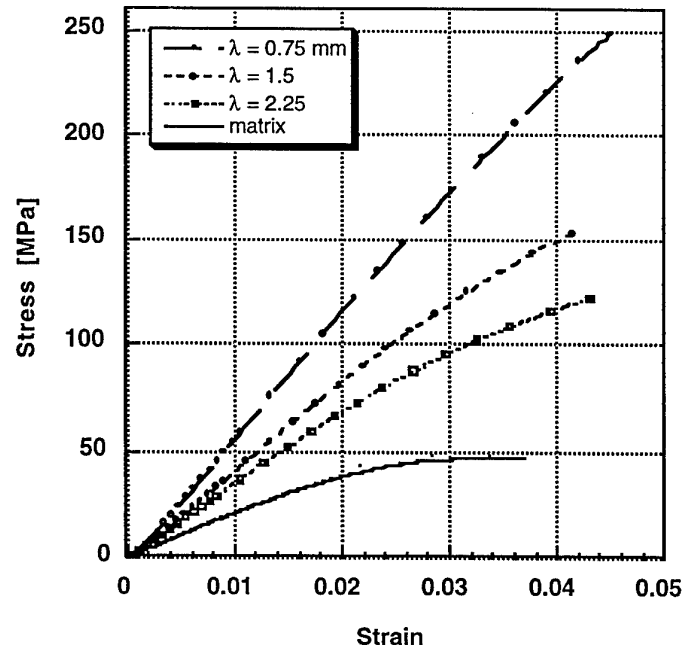
Figure 3.1   Stress-strain curves for notched monolayer specimens.
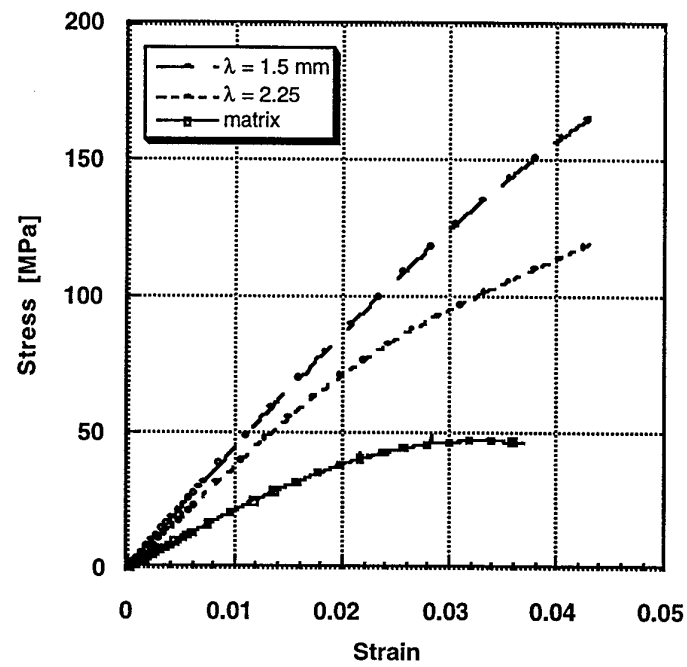
Figure 3.2   Stress-strain curves for dog-bone monolayer specimens.

(a)

(b)

Displacement, mm
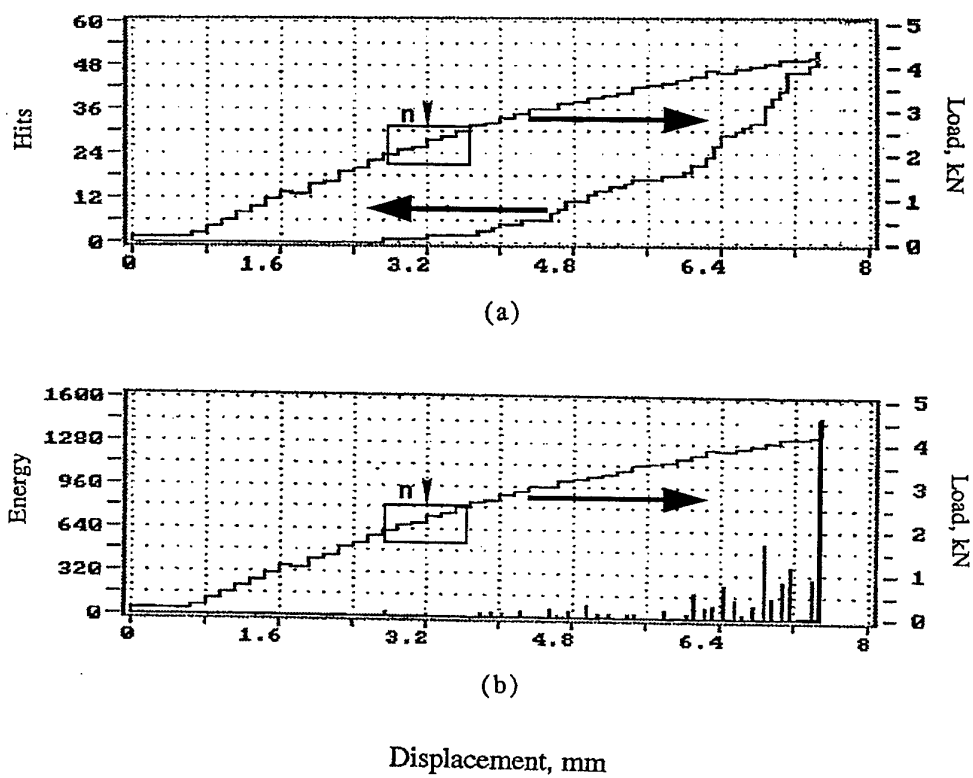
'n' denotes onset of non-linear stress-strain behavior

Figure 3.3   Acoustic emission hits and energy for a dog-bone monolayer specimen.

30
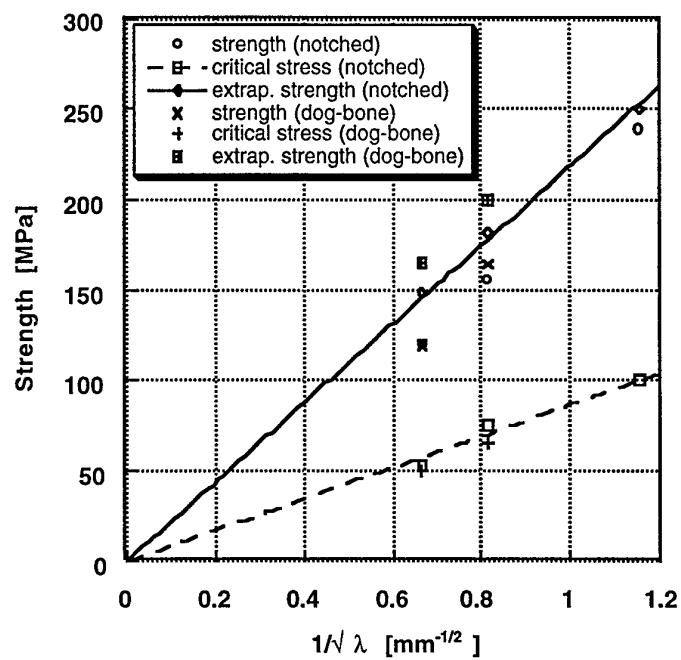
Figure 3.4   Critical stress and strength as a function of fiber spacing for the monolayer fiber architecture.
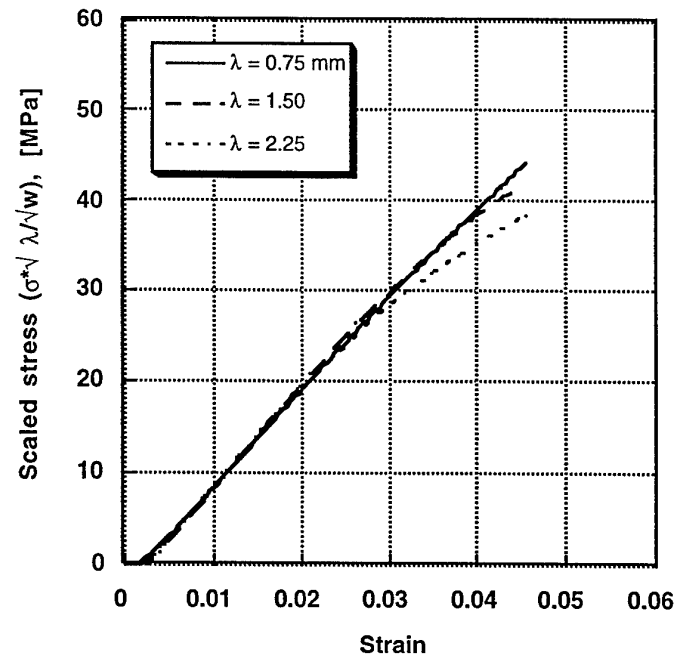
Figure 3.5   Scaling behavior of stress-strain curve for notched geometry.

32
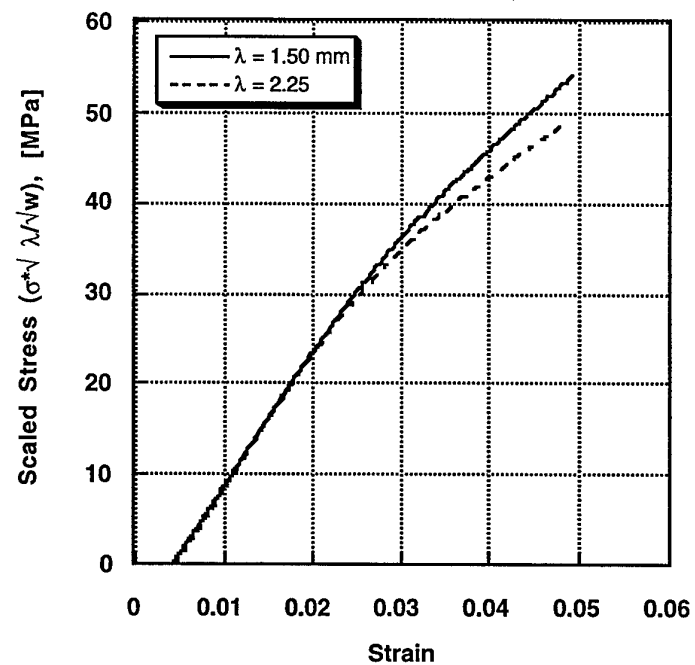
Figure 3.6   Scaling behavior of stress-strain curve for dog-bone geometry.
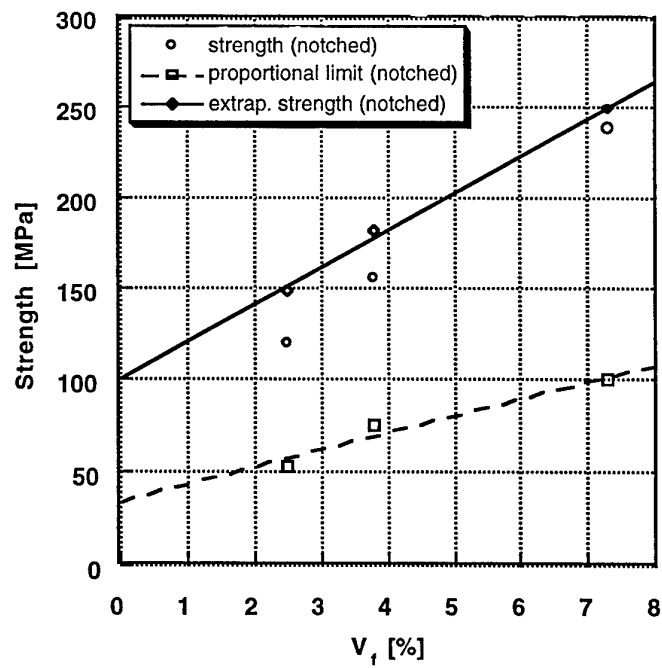
Figure 3.7   Critical stress and strength as a function of fiber volume fraction for monolayer specimens.
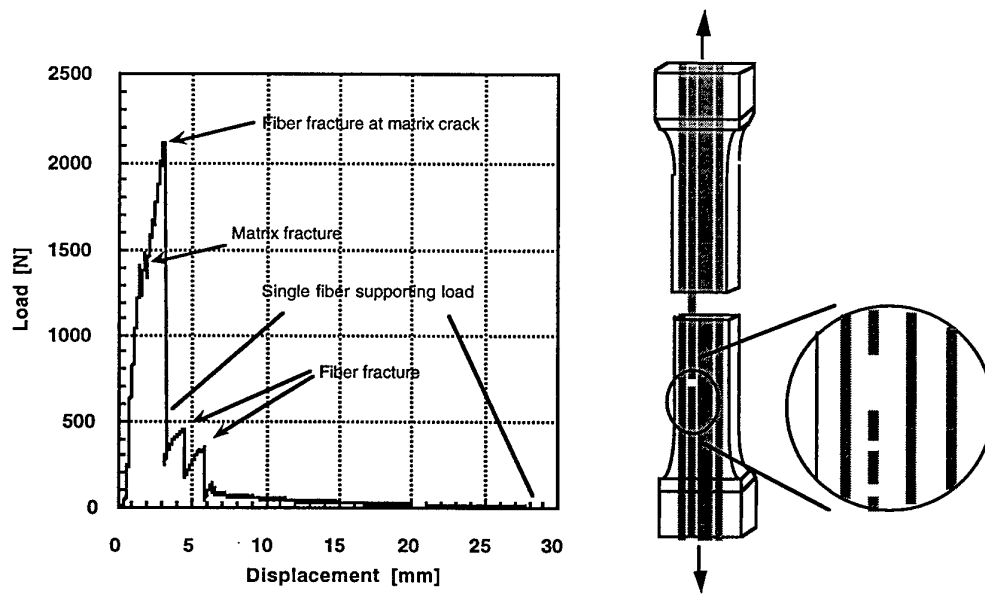
Figure 3.8   Load-displacement curve for pull-out of a single fiber in a dog-bone specimen.
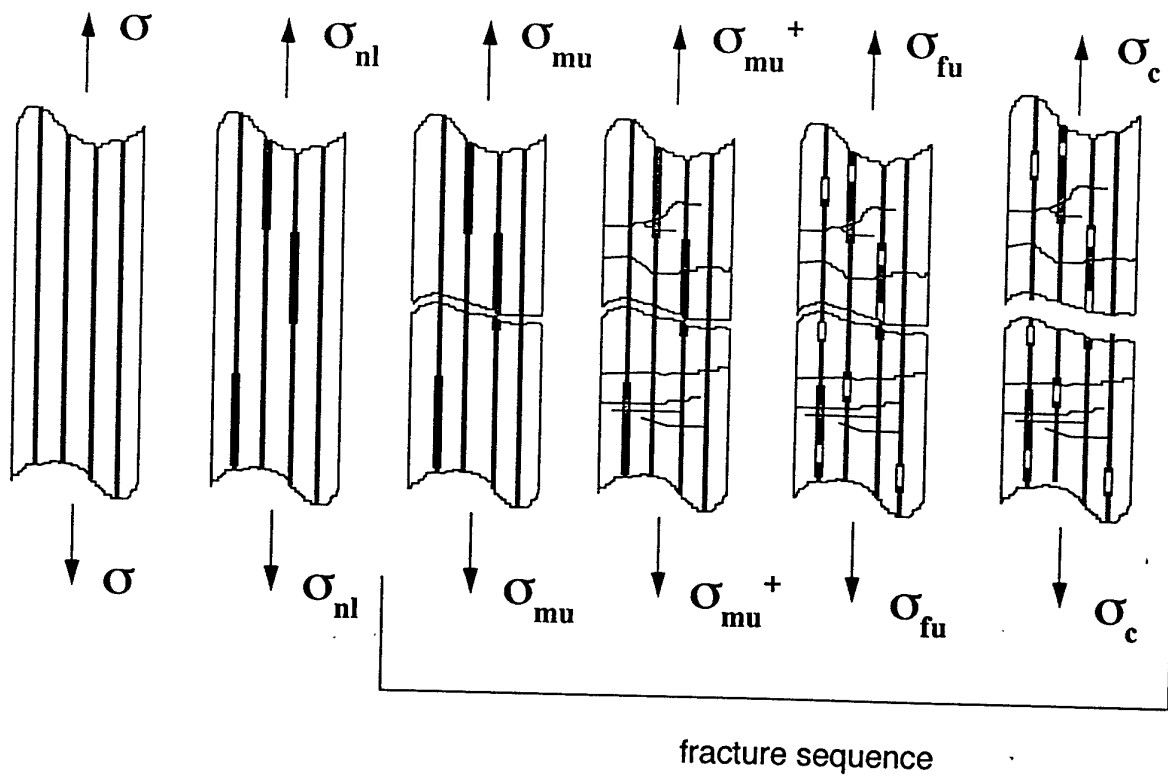
Figure 3.9   Proposed fracture process for monolayer fiber architecture specimens.

fibers

fracture initiation location

Figure 3.10   Typical fracture surfaces for monolayer fiber architecture specimens. Arrows indicate fibers.

4 MULTILAYER FIBER ARCHITECTURE

4.1 Introduction

In this chapter the results on the mechanical properties and fracture behavior of specimens with a multilayer fiber architecture, are reported.

In a similar manner to the investigation of the previous chapter, the mechanical behavior of the specimens, in this case the load-displacement response, was investigated through visual observation and acoustic emission methods during a single-ramp loading conditions. Again, the elastic response of the specimens, as well as the on-set on non-linear stress-strain behavior, and the ultimate strength of the specimens were found to be a function of fiber spacing, yet with a slightly different model than was found for the monolayer fiber architecture. The fiber-matrix interface was found to play a more important role in the multilayer architecture than the monolayer architecture.

To investigate the behavior of the interface more closely, two compact tension specimens with monofilament glass fibers at x-direction fiber spacing of 1.5 and 2.25 mm were tested using a dual-ramp loading loop and acoustic emission methods (Figure 2.8).

Post-failure analysis of the fracture surfaces revealed evidence of an adhesive bond between the fiber and matrix, as well as a distinct transition from slow crack to dynamic crack growth.

4.2 Experimental Observations

For this system a more detailed investigation was conducted. As seen in the following paragraphs, two loading waveforms were investigated with this system. A single-ramp loading waveform of 1 mm/min. was used with CT specimens defined by a characteristic length, w, of 32 mm and a thickness, B, of 8 mm. The fiber architecture of these specimens consisted of a constant y-direction fiber spacing of 1.5 mm and four x-direction spacing of 0.75, 1.5, 2.25 and 3.0 mm. A second loading waveform, referred to as unloading-loading or dual-ramp, was used in conjunction with acoustic emission methods. These compact tension specimens were defined by a characteristic length of 24 mm and a thickness of 8 mm and two x-direction fiber spacing, 1.5 and 2.25 mm, were investigated. For the dual-ramp waveform, the displacement of the initial loop was 1mm and was increased in increments of 0.5 mm for each subsequent loop until fracture.

4.2.1 in-situ observations

In-situ observation of the crack tip during single ramp loading was made using an optical microscope at 80X magnification. At approximately 400 N slow growth of the crack tip was observed, box I in Figure 4.1. As the crack tip extended, but before it reached the first fiber row, changes in the optical properties along the first row of fibers were observed. This change indicated the initiation of damage processes at the fiber-matrix interface. Damage of the interface began in the crack plane and gradually propagated in the z-direction along the fibers. As the crack reached the first fiber row, damage was initiated at the second row of fibers. Non-linear load-displacement behavior was noted during the damage process, region II in Figure 4.1.

Crack growth in the x-direction was arrested at, or within a few tenths of a millimeter after the first fiber row. As the load increased past the point of initial crack arrest the crack began to propagate in the z-direction. Bending of the specimen slowly opened the crack in the z-direction causing a 'peeling' action between the ligament and the 'front' section of the specimen. The load decreased slightly during this action, region III, before fast crack growth occurred in the z-direction. Fast fracture followed a curved path in the z-direction until the specimen separated into two or three pieces.

Damage at the fiber-matrix interface during loading was due to separation of the fiber and matrix. As the crack tip approached the first row of fibers, the stress state at the crack tip induced normal and shear stresses at the fiber-matrix interface. These normal and shear stresses induce fiber-matrix separation and sliding, respectively. This process was well explained by Gordon (Cook and Gordon, 1964), hence this process is referred to as the Gordon mechanism. In composites which possess an interface shear strength to composite tensile strength ratio less than 1:5, fiber-matrix separation is the dominate damage process, Figure 4.2 (Hull 1981). It has been shown in chapter 3 that this composite system does possess a weak interface. Therefore, it was concluded that the change in optical properties along the fibers during loading was due to fiber-matrix separation.

Further evidence of a weak fiber-matrix interface, hence fiber-matrix separation, was found during SEM analysis. An adhesive bond is one in which no chemical interactions between two adjoining surfaces occurs. In this case the surfaces are held together by friction or residual stresses. When these surfaces separate, i.e. when adhesive failure occurs, there is little damage to either surface. Figure 4.3 shows evidence of an adhesive bond between the fiber and matrix.

Post-mortem analysis of the fracture surfaces revealed a transition point from slow to dynamic crack growth on the y-z crack surface. Slow crack growth was characterized by a 'hackled' but planar surface while fast fracture was characterized by a relatively smooth but highly curved surface, Figure 4.4. This transition point was observed in all specimens, indicating that the fracture mechanism was independent of the fiber architecture.

Other authors have observed similar fracture morphologies in epoxy matrix composites. A 'scalloped' fracture morphology (Bradley and Cohen, 1985) can suggest coalescence of microcracks or a 'serrated' fracture morphology (Gustafson and Selden, 1985) can suggest interlaminar shear and/or peeling stresses. It was concluded that the bending stresses, inherent to the compact tension geometry, caused microcracks, which were initiated by fiber-matrix separation, to coalesce along the y- and z-directions resulting in the hackled surface morphology. Once a critical threshold of microcrack coalescence was reached the crack propagated dynamically in the z-direction.

4.2.2 mechanical properties

Experimental load-displacement curves for single ramp loading of the unreinforced matrix and composite compact tension specimens are shown in Figure 4.5. Observation of brittle behavior, i.e. linearity to fracture, for the unreinforced matrix indicated that plain strain conditions were present in these specimens. The unreinforced matrix displayed the highest stiffness. The stiffness of the composite specimens decreased with decreased fiber spacing, i.e. an increased fiber volume fraction. While it initially appeared contradictory that addition of fibers with a stiffness 30 times that of the matrix would decrease the composite stiffness, in-situ observations helped to clarify this result. Recall that separation of the fiber-matrix interface was observed during loading. As the fiber spacing was decreased, the number of fibers, and therefore the amount of fiber-matrix interface, was increased. Not only did this increase in interfacial area help to decrease the stiffness of the composite but it also increased ductility and toughness of the composite. The increased ductility of the initially brittle matrix material was apparent from the increased non-linear load-displacement behavior as a function of fiber spacing.

Toughness of the specimens, roughly 1/2 of the peak load times the displacement to failure, increased with a decreasing fiber spacing. This indicated that the composite indeed took advantage of the increased interface area by absorbing as much energy as possible through separation and/or sliding of the fiber-matrix interface.

During estimation of specimen toughness it was noticed that the peak load carried by each composite was fairly constant with respect to fiber spacing. This, again, was an initially

39

suprising result. However, nominal stress calculations for the compact tension geometry take into consideration the crack length of the specimen (equation 1.1).

4.2.3 acoustic emission evaluation

Although visual observations suggested that separation, and possibly sliding, of the fiber-matrix interface was the controlling factor for the mechanical behavior of the composite specimens, a measure of the damage as a function of loading and the interplay of interface damage and crack growth was investigated using acoustic emission methods.

While acoustic emission data can be used to locate the sources of acoustic activity in space as well as time, the quantitative values of this activity, e.g. amplitude, duration and energy, are generally not indicative of particular damage mechanisms (Daniel, 1993). Typically, friction, fiber debonding and fiber sliding are characterized by low energy events while delamination, crack growth and fiber fracture are characterized by higher energy events (Bunsell, 1979; Latishenko and Matiss, 1979). These signals often overlap making it difficult to separate the data on the basis of amplitude, energy, etc. Therefore, it is common practice to report acoustic activity qualitatively as cumulative acoustic events. The intensity of the activity is then taken as a proportional measure to the intensity of the damage.

Figure 4.6 and Figure 4.7 show the dual-ramp test load-time curves superimposed on the acoustic emission activity for specimens with fiber spacing of 1.5 and 2.25 mm, respectively. As both specimens investigated displayed similar behaviors, only the results from specimen with a 1.5 mm fiber spacing will be discussed.

In loading loop 'a' the maximum displacement was 1 mm. Low rate activity was observed at approximately 100, 450 and 800 N. The activity at 100 N was attributed to mechanical noise associated with the self-aligning specimen grips due to the presence of a similar peak when testing specimens of other geometries. Based on simultaneous visual observations, the activity at 450 and 800 N was attributed to crack growth initiation. This conclusion was supported by the behavior in loading loop 'b'.

In loop 'b' the maximum displacement was 1.5 mm. During this loop no activity was observed until 800 N. This was precisely the peak load reached in loop 'a'. This behavior, i.e. the absence of acoustic activity until some previous threshold load has been reached, is known as the Kaiser effect and is an important diagnostic tool for composite structures (Pollock, 1989). At this point the rate of activity was fairly constant until it ceased just after unloading. Note also that at approximately 800 N the load-displacement curve becomes non-linear. The onset of non-linearity at this load occurred in each subsequent loading loop.

In loop 'c' the maximum displacement was 2.0 mm. Activity began at 800 N, 200 N less than maximum load of loop 'b'. This observation coupled with that in loop 'b' of continued activity after unloading suggested that friction and separation of the interface had begun. Yet the activity rate did not greatly increase until 1000 N, the maximum load of the previous loop, which suggested that crack growth was still the dominate source of acoustic activity. Again, activity continued until just after unloading began.

A similar scenario was repeated in loop 'd' in which the maximum displacement was 2.5 mm. Activity attributed to interface friction and separation began at approximately 200 N and continued at a low rate until 1200 N where crack growth began. This loop again followed the typical pattern of no crack growth until the maximum load of was previous loading loop was reached. It was interesting to note in this loop that activity ceased prior to the maximum load. This may have been a sign of crack arrest at the first fiber row and possibly interface degradation to the point where the acoustic signals generated by friction and separation were now below the threshold level.

The acoustic behavior of loop 'e', in which fracture occurred, was quite unique. The programmed displacement was 2.5 mm but fracture occurred at 2.0 mm. At a load of only 200 N the greatest amount of activity was observed. Based on the behavior of previous loading loops it was concluded that the intensity of this activity burst was too high to be attributed to interface separation and friction but occurred at a load too low to be crack growth. From visual observations it seemed that this activity may have corresponded to the microcrack coalescence of the damaged interfaces. The activity spike at 1200 N was due to fracture but it was interesting to note that the specimen unloaded itself prior to reaching the programmed maximum displacement. This correlated well to the previous observation that the peeling behavior just prior to fracture was accompanied by a slight decrease in load.

As stated before the acoustic behavior of the specimen with a fiber spacing of 2.25 mm was similar to that just described with one interesting exception. Recall that the loading waveform during the dual-ramp testing was displacement controlled. Because of this, the higher stiffness of the specimen with a 2.25 mm fiber spacing resulted in a higher energy input into this specimen. Recall the energy input is equal to the area under the load-displacement curve. This higher energy resulted not only in higher levels of acoustic activity for equal displacements, relative to the specimen with a 1.5 mm fiber spacing, but also in fracture after only four loading loops, one less than for the 1.5 mm fiber spacing specimen.

4.2.4 strength

In § 3.3 it was shown that the critical stress for the onset of non-linear stress-strain behavior, or 'proportional limit', and the fracture stress (for uniaxially reinforced specimens of the same composite system used here) were functions of fiber spacing. The model which correlated stress to fiber spacing was

$$\sigma_c = \frac{\kappa}{\sqrt{\lambda}}. \tag{3.5}$$

This model was applied to the proportional limit and ultimate strength values of the multilayer specimens in the present investigation. Note that in the case of the multilayer specimens, the fiber spacing term, λ, in equation (3.5) must be replaced with the x-direction fiber spacing term, λ_x.

From the load-displacement curves the load at the onset of non-linearity and the peak load were used to find the (nominal) proportional limit and ultimate strength. The results of these nominal stress calculations as a function of the fibers spacing are shown in Figure 4.8. Each datum represents the average value of stress from specimens with a characteristic length of 32 mm and a particular fiber spacing. The error bars represent a ±10% deviation from the average values. Also note that the ultimate strength appeared to be sensitive to small initial crack tip to fiber distances, specifically the 'B' series specimens, Table 4-II.

It was observed that the previously proposed model described the multilayer data with the exception that for this geometry an intercept was observed. Hence, the model describing the two investigated stresses for the multilayer geometry is

$$\sigma_c = \sigma_0 + \frac{\kappa}{\sqrt{\lambda}_x} \tag{4.1}$$

where σ_0 = y-intercept,

κ = a constant term times fracture toughness for a given process, e.g. interface fracture toughness in the case of the critical stress, and

λ_x = x-direction fiber spacing.

Table 4-II   Experimental data for monofilament glass fiber multilayer specimens.

Specimen	Fiber Spacing, λ_x	Fiber Volume Percent, V_f	Specimen length, w	Initial Crack length, a_o	Crack Tip to Fiber, Λ	Fracture Toughness, K_{Ic}	Ultimate Strength, σ_c
Matrix1	n/a	n/a	36 mm	16.5 mm	n/a	3.31 MPa√m	34 MPa
Matrix2	n/a	n/a		16.5	n/a	3.14	32
Matrix3	n/a	n/a		16.4	n/a	3.38	35
Matrix4	n/a	n/a		16.6	n/a	3.21	33
A-a	0.75 mm	9.5 %	32	18.5	0.45 mm	10.95	136
A-b	0.75			18.3	0.50	10.73	137
B-a	1.5	5.0	32	19.2	0.85	8.29	111
B-b	1.5			19.0	0.30	11.14	148
B2-b	1.5			19.4	0.16	10.59	143
C-a	2.25	3.3	32	17.1	0.72	6.77	84
C-b	2.25			16.9	0.62	8.91	107
C-c	2.25			17.0	0.55	8.92	108
D-b	3.00	2.5	32	16.1	0.57	8.51	98
D-c	3.00			16.2	0.40	8.77	103
MB-a	1.50	5.0	24	†	†	n/a	n/a Dual Ramp
MC-a	2.25	3.5	24	15.5	0.50	n/a	n/a Dual Ramp

† fracture morphology prevented postmortem measurements.

While the physical significance of the intercepts, Figure 4.8, was unknown, the linear relationship describing the proportional limit as a function of fiber spacing extrapolated to approximately 35 MPa, only 2 MPa different than the nominal fracture stress found experimentally for the unreinforced matrix compact tension geometry. Even more interesting were previous results obtained for multilayer E-glass reinforced epoxy, Figure 4.9, which showed that the fracture stress depended on the fiber spacing according to equation (3.5), i.e. the line was observed to be through the origin (Zhao, 1996). The key to understanding the difference in behavior between the two systems was in the external geometry of the systems. In the previous work the external geometry of the compact tension specimens varied with fiber spacing, whereas for the present study the external geometry was kept constant. Indeed, it was shown through numerical modeling of the previous system that the linear relationship of equation (4.1) could be maintained while the intercept varied as a function of external geometry (Beldica, 1996).

Investigations of strength as a function of a characteristic length in ceramic materials (Rice, 1972; Carniglia, 1972) have also yielded relationships similar to equation (4.1), some with a zero and some with a non-zero intercept. For ceramic materials the important length scale is the grain size, G. Even for these well studied materials there are various theories as to the physical significance of the intercept.

The ROM is a popular model used to predict properties of a composite material, e.g. modulus or strength, based on the properties of the individual constituent materials and their relative

volume fractions. This model is based on uniaxially reinforced specimens under iso-strain loading conditions and therefore is not applicable to the present system. However, for the sake of comparison, the proportional limit and ultimate strength of the multilayer specimens was plotted as a function of fiber volume fraction, Figure 4.10. Again, a linear relationship according to equation (4.1) was observed. Yet, for reasons discussed in § 3.4, the prediction of composite strength as a function of fiber volume fraction may be appear to be valid, it suffers from certain limitations.

Finally, in § 3.3 it was observed that the stress-strain behavior of the monolayer geometry scaled with the fiber spacing according to $\sqrt{\lambda}/\sqrt{w}$. An attempt to scale the load-displacement curves of the multilayer CT geometry by the same scaling factor did not lead to similar results.
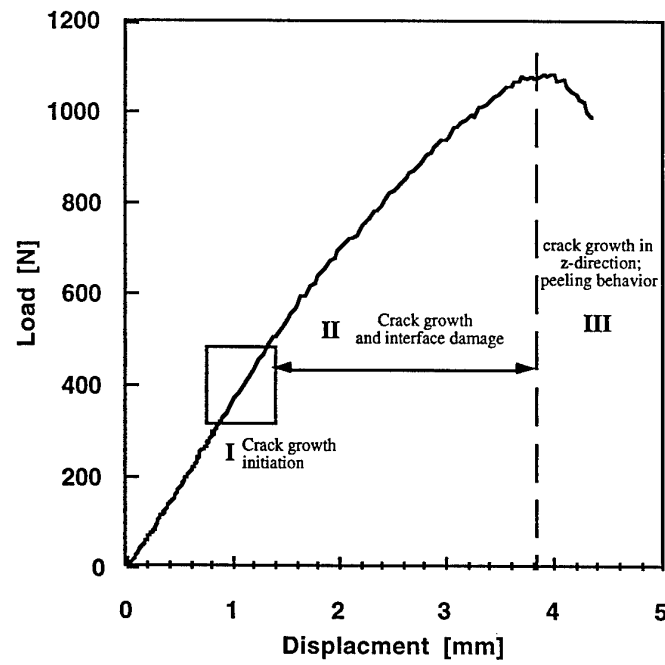
Figure 4.1   Damage regimes for loading of a monofilament glass fiber reinforced multilayer fiber architecture compact tension specimen.

initial
crack

Λ

a_o

slow
growth

a_1

fiber
debonding
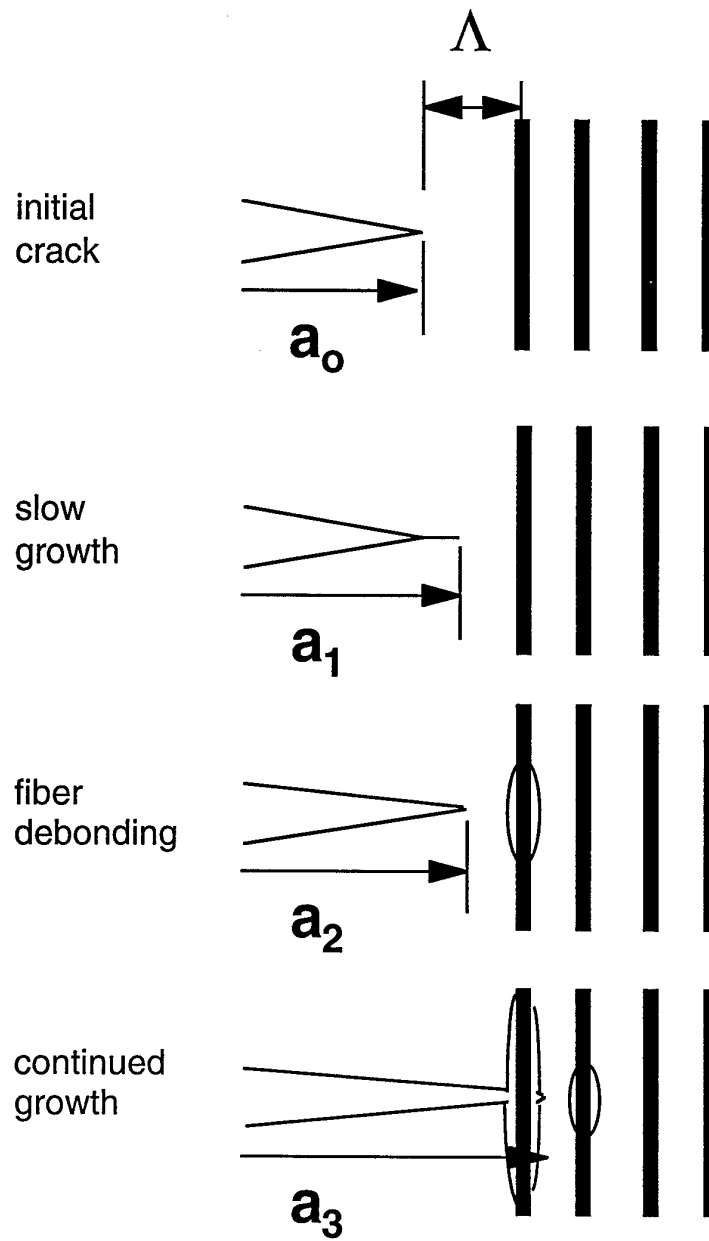
a_2

continued
growth

a_3

Figure 4.2   Schematic of Gordon mechanism for composites with a weak fiber-matrix interface.

damage free fiber surface indicates
adhesive failure of
fiber-matrix interface

16kV   ESD   ×125   D=9.4mm P=5.0T
UIC Material Lab   95.08.29 R1
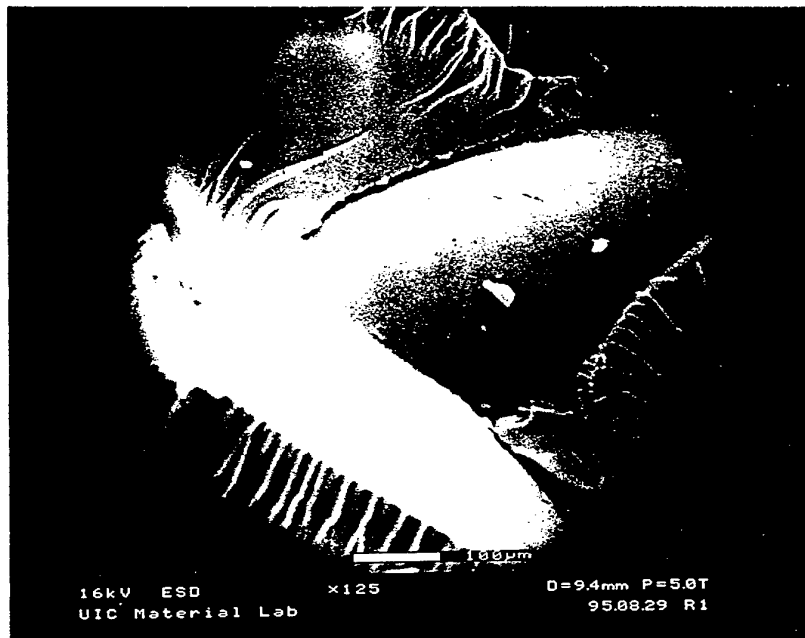
Figure 4.3   SEM photograph showing evidence of an adhesive bond between the fiber and matrix.

slow crack growth 'hackled' region
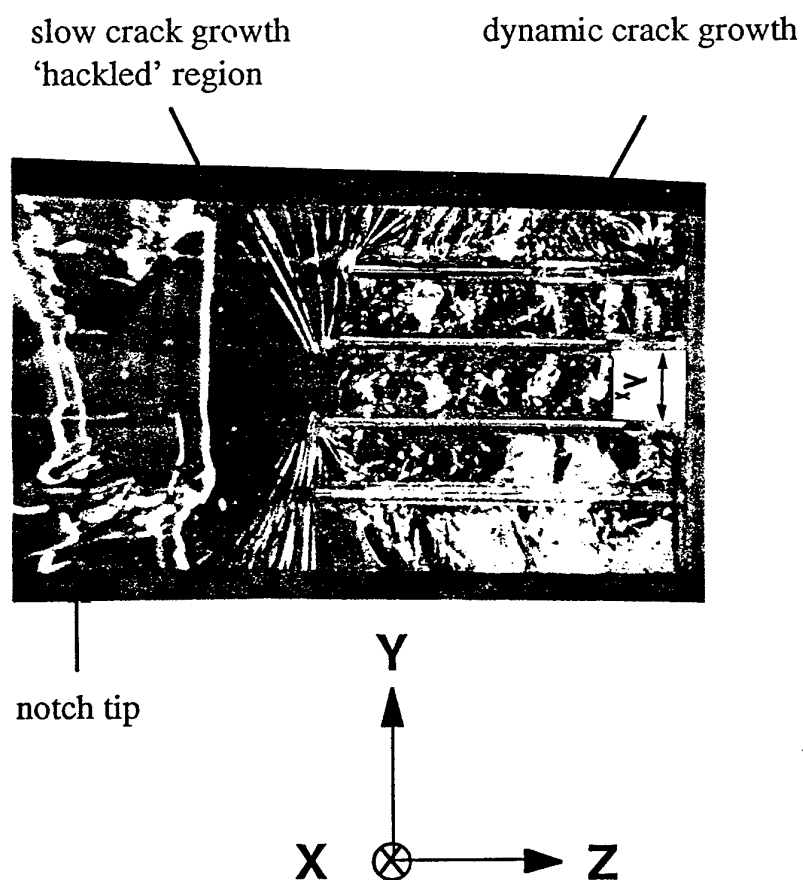
dynamic crack growth

notch tip

Y

X ⊗ → Z

Figure 4.4   Photograph of y-z fracture surface for monofilament glass fiber compact tension specimens.
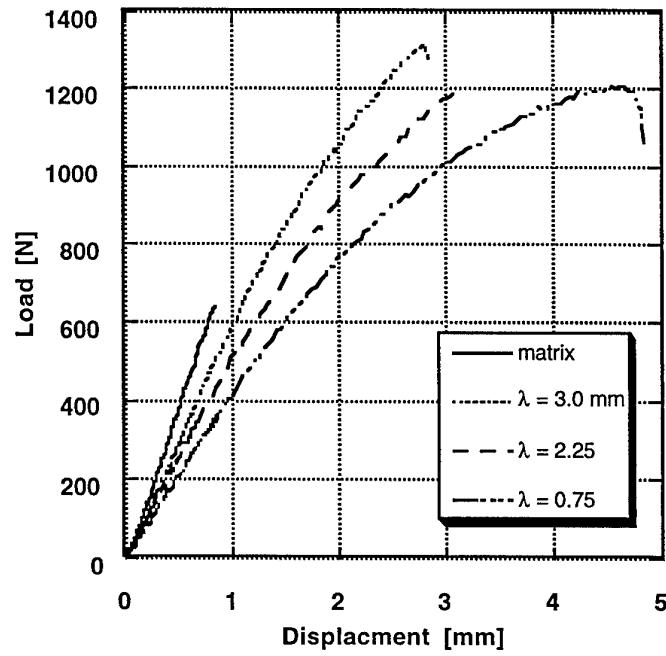
Figure 4.5   Load-displacement curves for monofilament glass fiber compact tension specimens.

Hits

Load [kN]

(a)

(b)

(c)

(d)

(e)

mechanical noise

onset of crack growth

onset of sliding/friction

fracture

Time [s]

Figure 4.6   Acoustic emission response of a monofilament glass fiber reinforced specimen with a 1.5 mm fiber spacing under dual-ramp loading at 1 mm/min.

49

Hits   **Load [kN]**

(a)

(b)

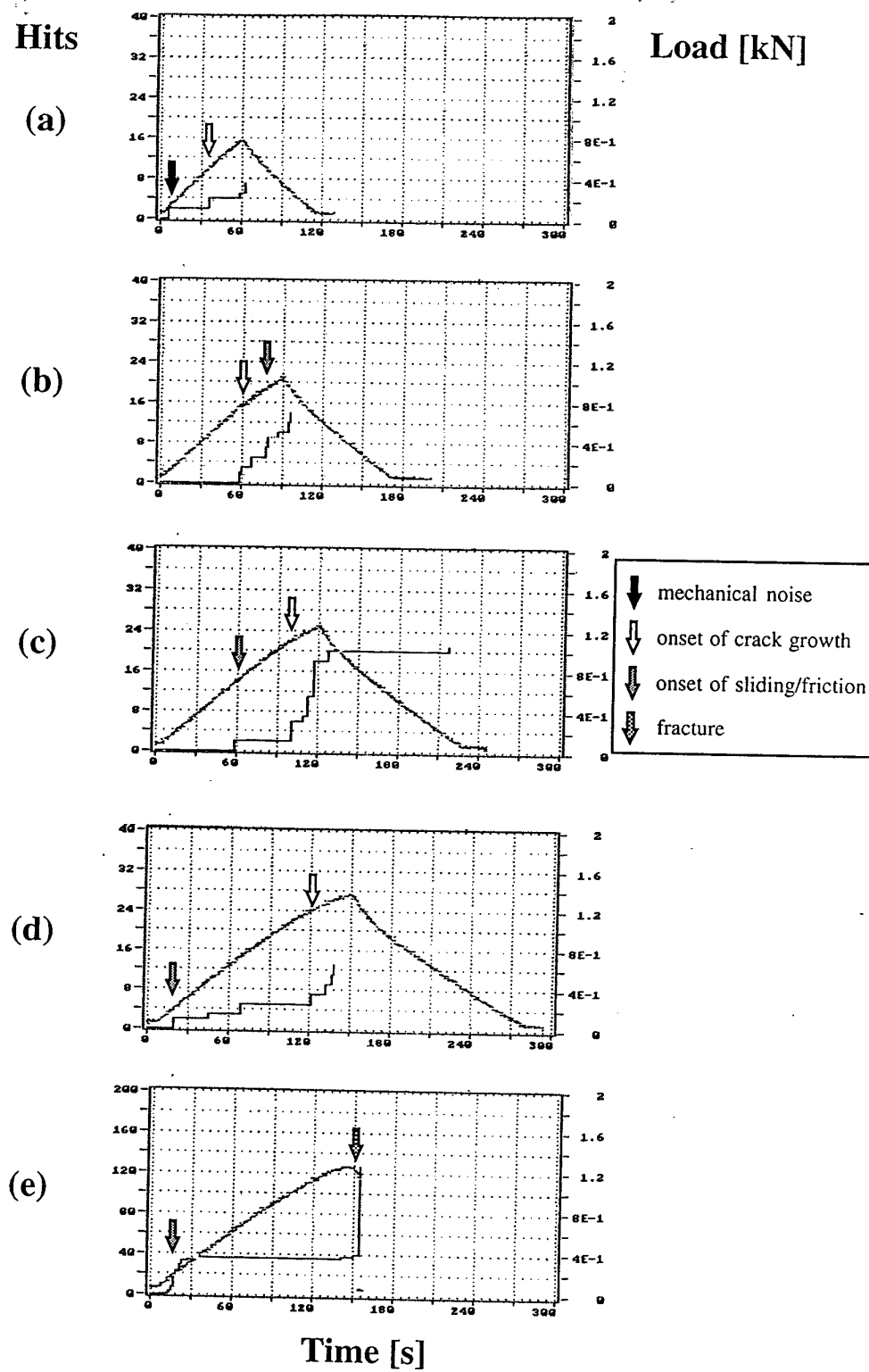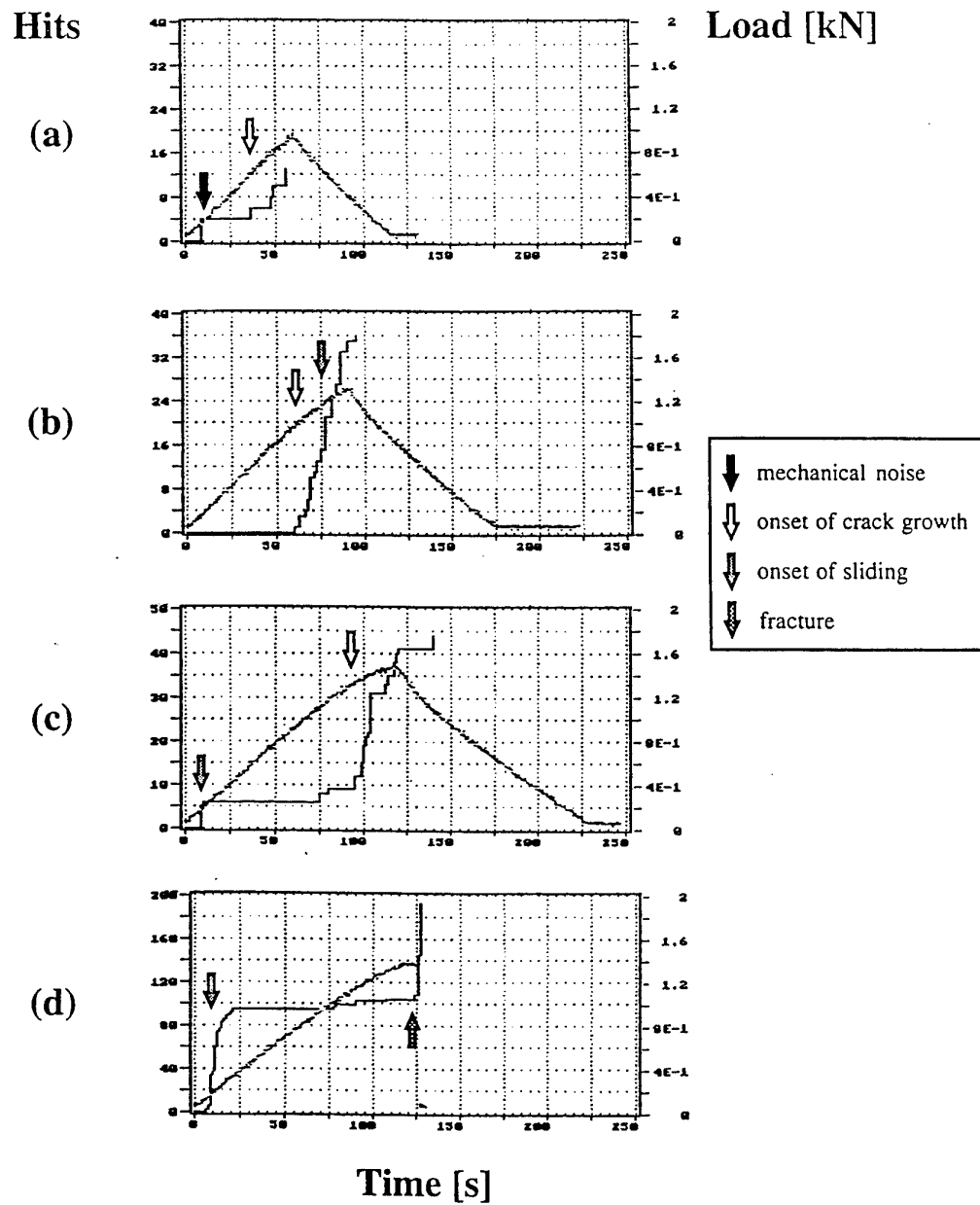|	
▼	mechanical noise
⇩	onset of crack growth
⬇	onset of sliding
⬇	fracture

(c)

(d)

Time [s]

Figure 4.7   Acoustic emission response of a monofilament glass fiber reinforced specimen with a 2.25 mm fiber spacing under dual-ramp loading at 1 mm/min.

50
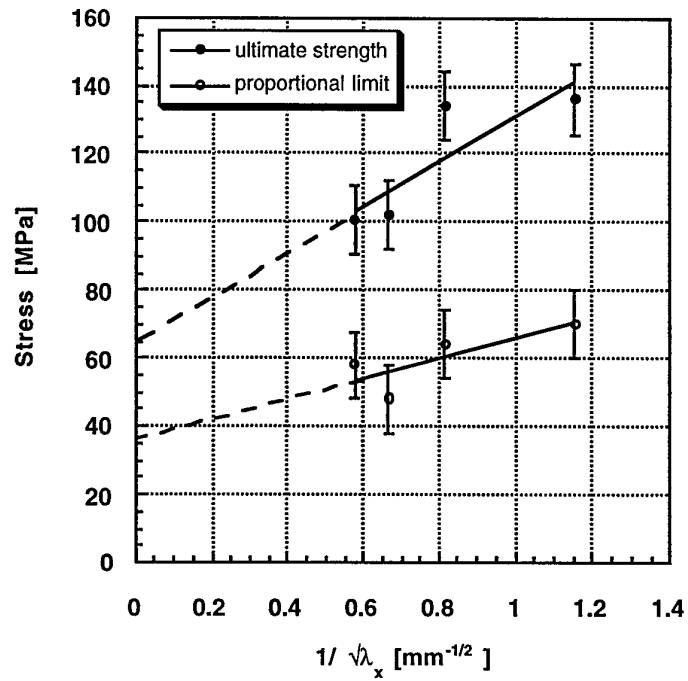
Figure 4.8   Average critical stress and ultimate strength values as a function of fiber spacing for monofilament glass fiber multilayer specimens.

Figure 4.9　　　Ultimate strength as a function of fiber spacing for an E-glass/epoxy multilayer system in which the external dimensions of the compact tension specimens changed with fiber spacing (Zhao, 1995).
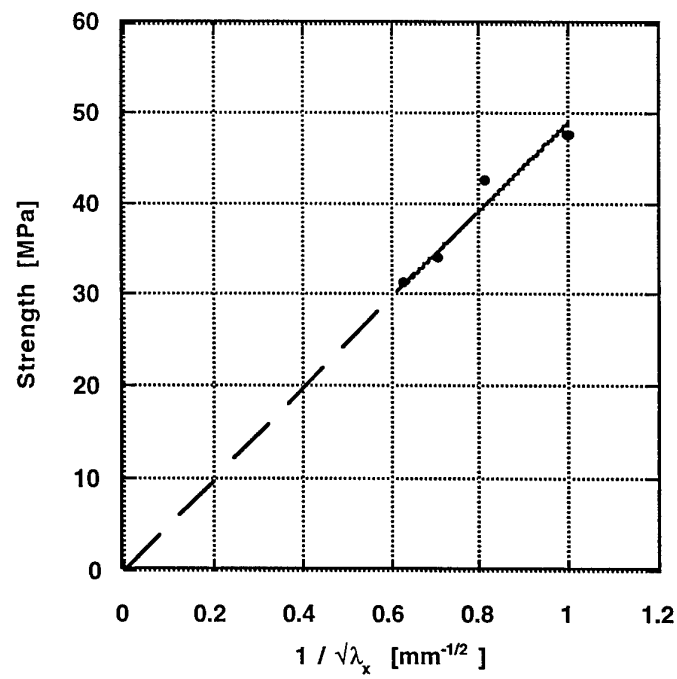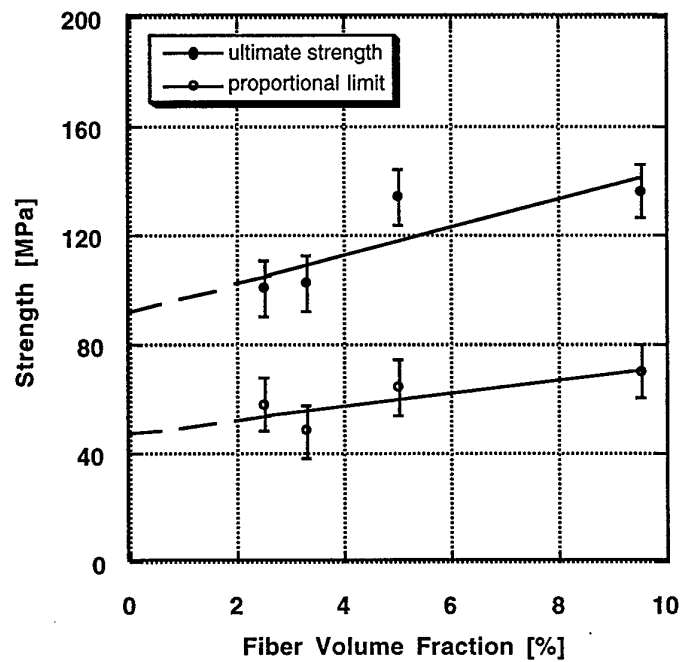
Figure 4.10   Critical stress and ultimate strength as a function of fiber volume fraction for monofilament glass fiber reinforced specimens.

5 NUMERICAL ANALYSIS

5.1 Boundary Element Method

Finite Element Methods (FEM) are well known and often used numerical modeling procedures for stress distribution in two or three dimensions. However, these methods are often time consuming in mesh preparation and computing time. A second method, Boundary Element Method (BEM), has clear advantages over FEM in some respects. These include discretizing only the boundary of a body, fewer equations to solve (hence more efficient computing). The BEM is especially suited to handle linear elastic materials and 2-dimensional models (Wearing et al., 1990). In the BEM, tractions and displacements are the basic variables. One set of these variables is prescribed while the second set is solved for, usually via integration of the appropriate equations.

A BEM simulation code was developed by this research group (Beldica, 1996) to numerically model the fiber architectures that have been investigated experimentally. Of particular interest was the potential to model the multilayer fiber architecture specimens. As stated, BEM is an efficient way to model a 2-dimensional representation of a body. By discretizing a CT specimen in two dimensions a large parametric study of the internal fiber architecture could be undertaken. After extensive initial studies, discussed by Beldica, the simulation was applied to the multilayer monofilament glass fiber reinforced specimens investigated in chapter 4. While the details of the working code are not discussed here, it will be shown that the initial simulation code proved not only to agree with the experimental results but also shed light on some experimental results that were previously unexplained.

5.2 Simulation Method and Analysis

The BEM simulation was performed on a 2-dimensional representation of a CT specimen with a multilayer fiber architecture. A representative schematic on which the BEM was based is shown in Figure 5.1. Notice that the three-dimensional fiber row was simulated using a single reinforcement 'layer.' Beside the reduction of a 3-dimensional specimen into two dimensions, a perfect fiber-matrix interface was chosen to reduce the complexity of the interaction between the elements. The nomenclature used in the schematic and also throughout this chapter are defined below:

w = characteristic length of the specimen,
a = initial crack length (note that both w and a are defined by ATSM E 399),
L = front edge to first fiber distance,
Λ = crack tip to first fiber distance,
λ = reinforcement layer spacing,
d = reinforcement layer thickness,
N = number of reinforcement layers,
E_r/E_m = ratio of reinforcement layer modulus to matrix modulus (in every case $E_m = 1$)
υ_f, υ_m = Poisson's ratio for the reinforcement and matrix material (in every case both are 0.3).

The BEM was used to calculate the strain energy at two crack lengths. The first crack length, a_1, corresponded to the initial crack length and the second crack length, a_2, corresponded to the initial crack length plus a step increment, i.e. $a_2 = a_1 + $ step. In every case the step increment was chosen as 0.1 mm. From the crack lengths and calculated strain energies the energy release rate for mode I crack growth could be calculated,

54

$$G = \frac{(U_2 - U_1)}{(a_2 - a_1)} \qquad (5.1)$$

where U_1 and U_2 are the calculated strain energies at crack lengths a_1 and a_2, respectively. Using LEFM, the SIF for mode I loading is defined as

$$K_I^2 = \frac{E'}{(1 - v^2)G}. \qquad (5.2)$$

Assuming a plane strain condition, E' and v are the Young's modulus and Poisson's ratio of the matrix, respectively. Note that the model assumed that crack growth occurred entirely in the matrix, as was observed experimentally, thus the use of the matrix elastic constants in equation (5.2). The stress intensity factor at various reinforcement configurations, as well as with various reinforcement elastic constants, was calculated and denoted as K_r. For every change in the BEM mesh, a homogeneous SIF, K_o, corresponding to a reinforcement with identical elastic properties as the matrix, i.e. $E_r/E_m = 1$, was also calculated. All calculated SIF values were normalized by the homogeneous SIF.

Next, the calculated SIF was correlated to a critical stress. From the Griffith criteria, the following relationship can be deduced,

$$\left(\frac{P}{B}\right)(K_r)_{P/B=1} = K_{mc} \qquad (5.3)$$

where
P = load,
B = specimen thickness,
K_r = reinforced SIF,
K_{mc} = fracture toughness of the matrix,

The ratio P/B can be calculated from equation (5.3) because K_r, the simulated SIF value, and K_{mc}, the experimental fracture toughness value, are known. Now, P/B can be used in equation (1.1) to calculate the 'critical' stress associated with the SIF calculated from the BEM simulations.

5.3 Parametric Study of SIF

5.3.1 single fiber reinforcement

A 2-dimensional CT model with dimensions, w, a and d, of 24, $0.45w$ and 0.4 mm, respectively, was reinforced with a single layer at various distances from the crack tip, Λ. The SIF (normalized) calculated for each position of the single fiber within the ligament for various reinforcement layer modulus values, 1, 2, 5 and 10, is shown in Figure 5.2. Note that a simulation with a reinforcement modulus of one was run in every case to check the stability of the mesh and also to generate a normalizing constant. For every reinforcement layer with a modulus greater than the matrix, i.e. $E_r/E_m > 1$, a similar reinforcing trend was observed.

As the reinforcement layer was moved to the center of the ligament the influence almost dropped to zero. As the reinforcement layer was moved through the center and into the rear portion of the ligament, the SIF was observed to decrease again, although to a much lesser

extent than for a fiber in the front portion of the ligament. Also, the decrease in SIF was more pronounced with an increase in the reinforcing layer modulus, i.e. stiffness.

Recalling previous discussions on the deformation behavior of a CT specimen under loading, the SIF behavior near the center of the ligament can be explained. It is known that during bending of a beam there exists a neutral axis at which the stresses and strains are zero. Apparently the bending of the CT ligament under loading created a neutral axis in the region between 40 and 60% of the ligament length. That is, the stiffness properties of the reinforcing layer could not be realized in this region due to the low stresses near the neutral axis. However, a slight decrease in SIF was still observed in this region as E_r was increased due to the overall stiffening effect of the reinforcement layer.

This general increase in ligament stiffness with E_r was also observed when the reinforcement layer was moved into the rear of the ligament. In this region the effect of the reinforcement on SIF could only be realized through stiffening the ligament against compression, hence lowering the tension and therefore crack tip SIF at the front of the ligament. Note the large difference in SIF decrease. In the front of the crack tip, reduction of the SIF as explained by LEFM led to an almost a 30% reduction in SIF for the stiffest reinforcement. However, for a reinforcement with the same stiffness located near the specimen rear edge a less than 10% decrease in SIF was achieved.

5.3.2 multiple fiber reinforcement at a variable layer spacing

Naturally the next step was to increase the number of reinforcement layers in the ligament in order to understand the interaction and combined effect of the fibers on the SIF. At this point the possibilities for reinforcement architecture became very large. Although several architectures were investigated, only the simulations that related to the experimental systems investigated in this work will be discussed. Two simulations were run for specimens with five reinforcement layers at spacing of 1 and 2.25 mm. The results are shown in Figure 5.3.

The interaction effect on SIF between the reinforcement layers for the multiple reinforcement architecture was investigated jointly with Beldica. Simulations were run with single reinforcement layers at increments of 2.25 mm starting from a position 3.2 mm from the crack tip. The individual effects on SIF from each of these simulations were added together and compared to the results already displayed in this section. Figure 5.4 shows the results of the superposition of these individual reinforcing effects on the SIF. It was observed that, up to a reinforcement modulus of 10, the effect of a five fiber reinforcement could be described by the superposition of the SIF effects of single reinforcement layers located at the same locations. It appeared that any interaction between the layers for a multiple reinforcement architecture would not become important, i.e. a deviation from the superposition of greater than 10%, until the reinforcement modulus became over 10 times greater than the matrix modulus. However, note that for glass-reinforced polymers, E_r/E_m is typically on the order of 20, therefore interaction effects may become significant at this ratio.

5.4 Simulation of the Experimental Results

The next study involved the simulation of the experimental results on the monofilament glass fiber reinforced CT specimens. The experimental values of the fiber and matrix moduli, 66 and 2.2 GPa, respectively, were used so that direct comparison to the experimental results could be made. Again the external dimensions of the specimen were based on a characteristic size, w, of 24 mm. This simulation not only calculated the reduction in SIF due to the reinforcement but also used the method of §5.2 to calculate the critical stress at the crack tip for a crack extension of 0.1 mm. In addition, two possibilities for the way in which the crack tip may 'feel' the reinforcement layers were investigated. In the first case, the ligament was reinforced by 'discrete' layers, physically similar to discrete fibers, in the second case, the discrete architecture was transformed into an 'effective' architecture in which the ligament was represented as a monolithic reinforcement with a stiffness found from the ROM.

56

5.4.1 discrete architecture

In these simulations the E_r/E_m ratio for each discrete layer was calculated based on the fiber rows of the experimental specimens. The experimental stiffness constants and the ROM were combined using the geometry of Figure 5.5. A discrete reinforcement layer E_r/E_m value of 13.85 GPa was calculated from the experimentally determined elastic constants. Recall that fiber spacing of 3.0, 2.25, 1.5 and 0.75 mm were investigated experimentally. However, due to BEM mesh construction limitations only discrete reinforcement spacing of 3.0, 2.25 and 1.5 could be simulated.

Although the reinforcement layer modulus corresponding to the experimental geometry had been calculated, the first step of the simulation was to investigate the decrease in SIF over a range E_r/E_m, Figure 5.6. Note that in this parametric study, a E_r/E_m ratio of less than unity was also modeled. In the region of $E_r/E_m > 1$ the expected trend was observed, the SIF decreased with reinforcement spacing for a given stiffness ratio and the decrease in SIF was greater for all reinforcement spacing as the stiffness ratio increased. In the region of $E_r/E_m < 1$ the opposite trends were observed. This response was predicted by LEFM in that an inclusion less stiff than the matrix ahead of the crack tip would cause an increase in SIF. Also, in general the overall stiffness of the ligament would decrease for a less stiff 'reinforcing' layer causing an increase in SIF.

Next the crack tip stress value at $E_r/E_m = 13.85$ was calculated for each reinforcement spacing. Using the resulting K_r value in equation (5.3), solving for P/B, then using equation (1.1), the nominal stress at the crack tip for the model with a crack length of a_2 was found, Figure 5.7.

5.4.2 effective architecture reinforcement

Throughout this work the use of fiber spacing as a characteristic size for composite behavior has been argued. However, how the crack tip actually 'sees' the ligament is an interesting question. Are the reinforcements ahead of the crack tip truly discrete influences on the crack tip or is the ligament seen as a monolithic single phase with an overall or 'effective' stiffness?. The BEM analysis offered a simple way to compare the numerical results of these two possible types of influence. The first type, a discrete reinforcement architecture, was as discussed in the previous section. The second type, the ligament acting as a single phase with a modified or 'effective' modulus, is the subject of this section.

The effective modulus, E_{eff}/E_m, for this model corresponding to each reinforcement spacing was found by applying the ROM to the 2-D ligaments of the discretely reinforced models. The dimensions of the ligament were taken from crack length + Λ to the rear of the ligament, or 12.4 mm, in the x-direction and the entire height of the specimen, i.e. $w*1.2 = 28.8$ mm, in the y-direction. In this way the effective architecture models could be correlated to discrete reinforcement spacing of 3.0, 2.25 and 1.5 mm. Recall that due to mesh generation limitations a discrete spacing of less than 1.5 mm could not be modeled. But due to the fact that only one reinforcement layer was present in the mesh for the effective architecture, the effective modulus corresponding to any fiber spacing, could be modeled. This allowed a reinforcement fiber spacing of 0.75 mm to be simulated.

Again, the first step was to calculate the SIF over a range of E_{eff}/E_m values, Figure 5.8. The trend of an exponentially decreasing SIF was observed. The large decrease in SIF, over 70%, is due to the fact that E_{eff}/E_m corresponds to the modulus of stiffness of the entire ligament, not reinforcement layers from which the stiffness was calculated.

The critical stresses for these simulations were calculated in the same manner as for the discrete architecture. Note that in the case of the discrete architecture, each K_r was taken at $E_r/E_m = 13.85$, however, for the effective architecture the value of E_{eff}/E_m differed for each reinforcement spacing, Table 5-I. The critical stress results for this architecture are also shown in Figure 5.9.

57

5.4.3 comparison of simulation critical stress to experimental strength data

The simulation parameters and critical stress results are summarized in Table 5-I. Note that, for the effective architecture, the same mesh was used for each simulation, hence only one value for K_o.

Table 5-I   Important BEM specimen parameters and results.

Modeled Geometry	Layer Spacing and Number, λ , N	Specimen Length, w	Crack Length, a	Crack Tip to Fiber, Λ	E/E_m or E_{eff}/E_m	SIF due to mesh, K_o	Critical Stress, σ_c
Matrix only	-	24 mm	10.8 mm	-	-	1.6608	36 MPa
Discrete Architecture	1.5 mm, 8 2.25, 6 3.0, 5	24	10.8	0.8 mm	13.85	1.7065 1.7000 1.6968	77 72 71
'Effective' Architecture	0.75, 12 1.5, 8 2.25, 6 3.0, 5	24	10.8	0.8	7.19 5.15 4.11 3.59	1.6608	80 71 64 61

Critical stress as a function of reinforcement spacing for each reinforcement architecture has been shown in Figure 5.9. For both architectures the critical stresses displayed a linear relationship with reinforcement spacing that could be described by the model proposed for the experimental critical stress or strength results, equation (4.1). Although slightly higher critical stress was achieved with the discrete architecture simulations, the main difference between the results of the two architectures appeared to be the slope of the linear relationship.

The difference between the simulated and experimental critical stress values were found to be 10% for discrete architecture simulation and less than 5% for the effective architecture simulation. Also, the slope of the strength vs. fiber spacing function for the effective architecture simulation was similar to that of the experimental relationship for strength. The correlation between the numerical model and experimental results was encouraging despite the fact that the simulation was performed using only a 2-dimensional model of the experimental compact tension specimens and that the model assumed a perfect fiber-matrix interface.
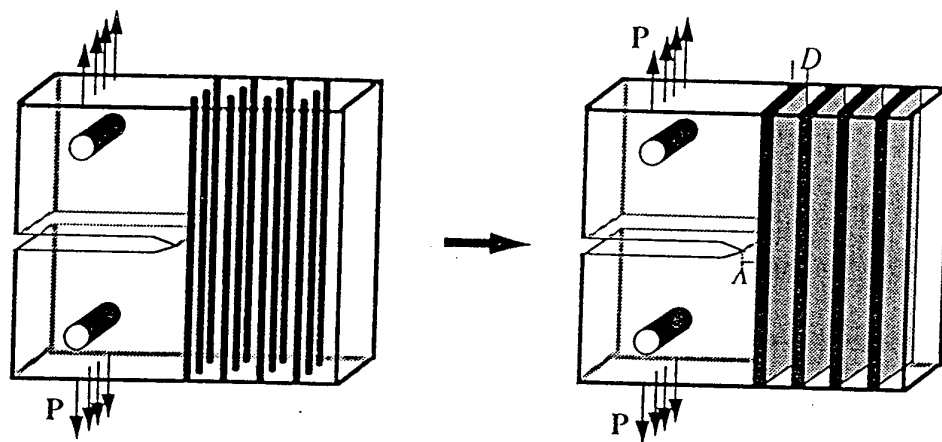
58

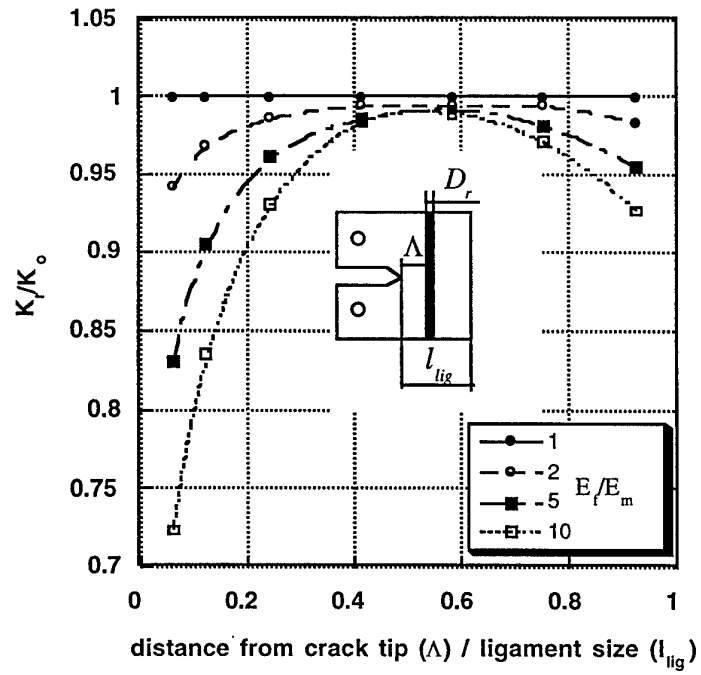Figure 5.1 2-Dimensional representation of a compact tension specimen.

Figure 5.2   Normalized SIF as a function of reinforcement layer location for various E_f/E_m ratios.
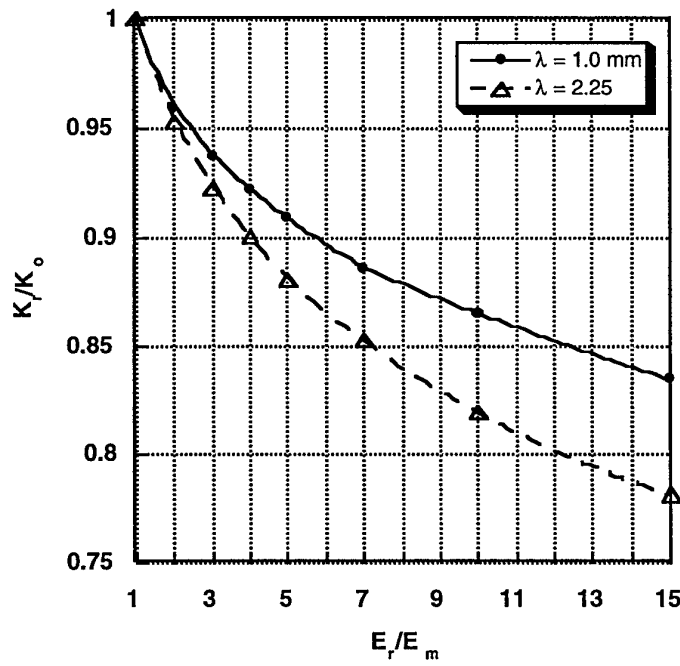
Figure 5.3   SIF reduction as a function of reinforcement modulus for two reinforcement spacing.
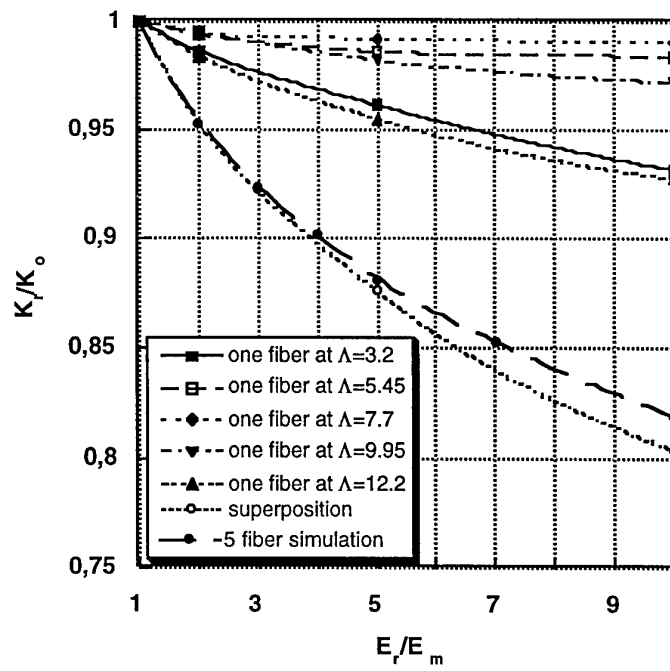
61

Figure 5.4   Superposition effect for SIF due to reinforcement of a single layer at different locations.
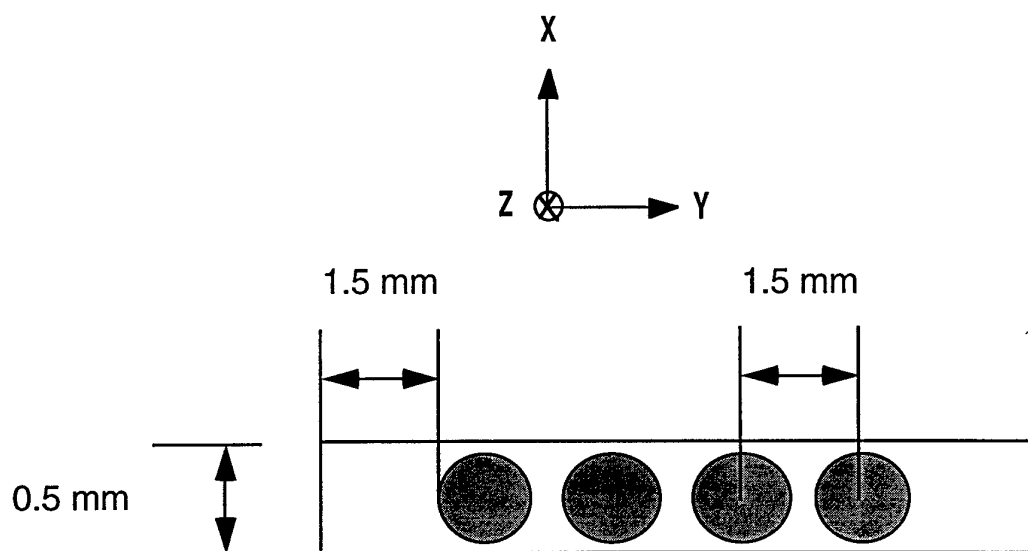
Figure 5.5   Experimental fiber row geometry used in combination with the ROM to calculate the modeled reinforcement strip.
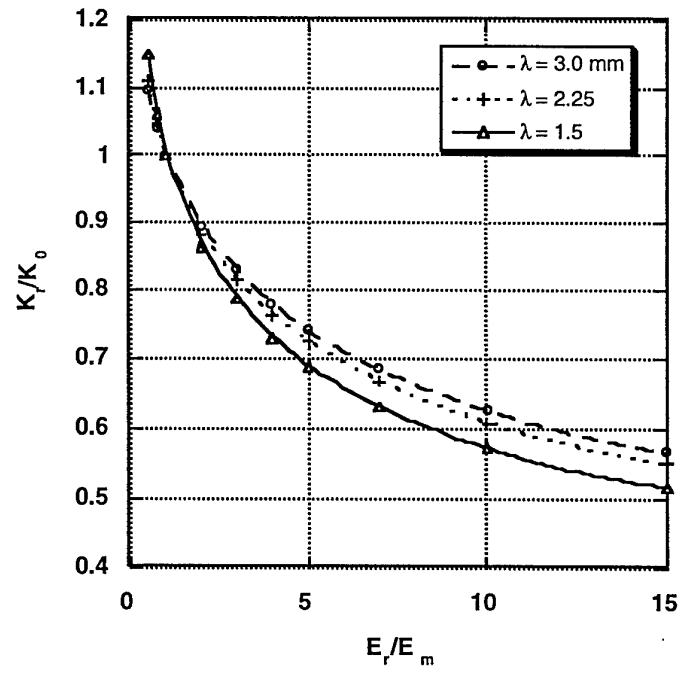
Figure 5.6   Normalized SIF as a function of fiber modulus for discrete reinforcement geometries.
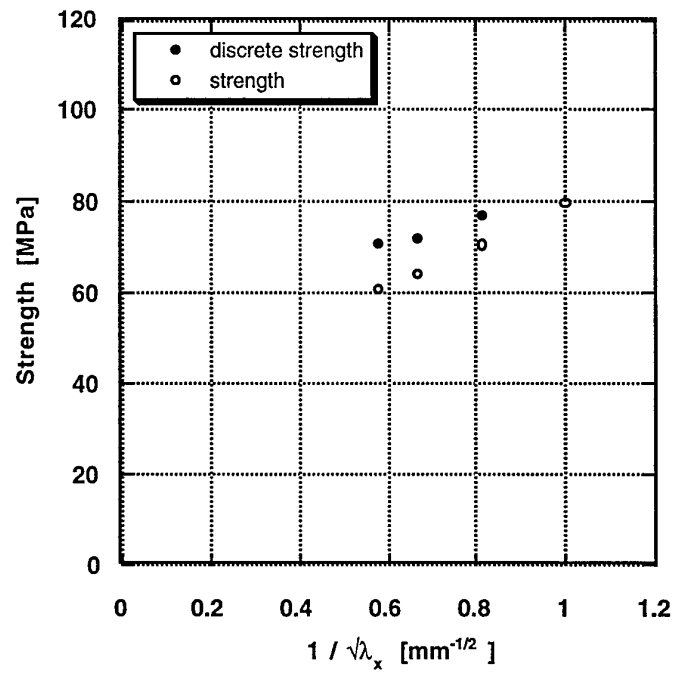
Figure 5.7   Critical stress calculations for discrete and effective simulations.
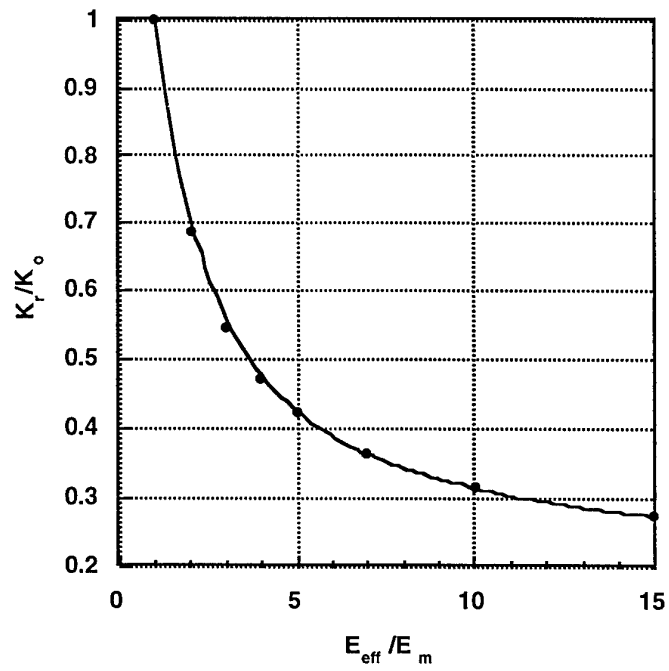
Figure 5.8   Normalized SIF as a function of fiber modulus for effective reinforcement geometry.
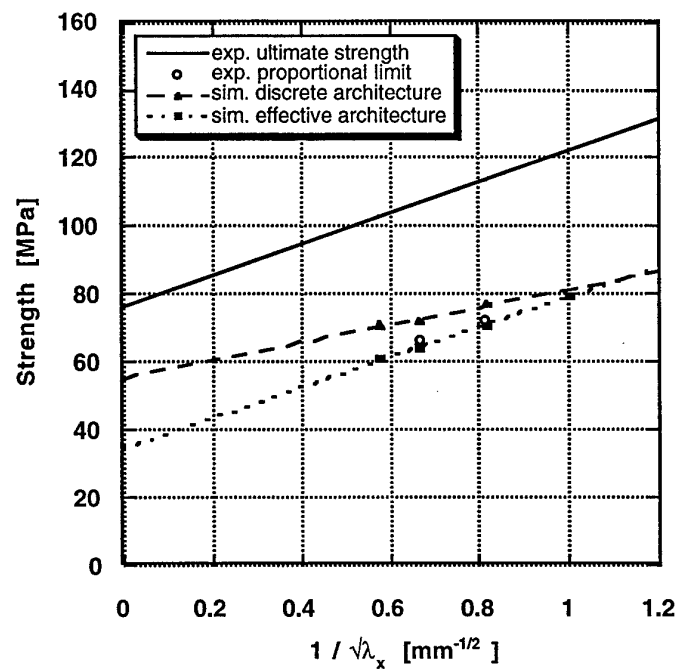
Figure 5.9   Comparison of simulated critical stress values to experimental values.

CITED LITERATURE

ASTM: Standard test method for plane-strain toughness in metallic materials. E 399-83, pp. 394-410 Philadelphia, ASTM, 1985.

Alturi, S.N. and Kobayashi, A.S.: Mechanical responses of materials. In: Handbook on Experimental Mechanics, ed. A.S. Kobayashi, pp. 1-38. New York, VCH Publishers Inc., 1993

Ashbee, K.: Fundamental Principles of Fiber Reinforced Composites. Lancaster, Technomic Publishing Inc., 1989

Aveston, J., Cooper G.A., and Kelly A.: The properties of fibre composites, Conf. Proc. Natl. Physics Lab. Nov.4 1971

Bar-Cohen, Y.: NDE of fiber-reinforced composite materials - A review. Materials Evaluation 44:446-454, 1986.

Bar-Cohen, Y. and Crane, R.L.: Nondestructive evaluation of fiber-reinforced composites with acoustic backscattering measurements. Composite Materials: Testing and Design (Sixth Conf.); ASTM STP 787, ed. I.M. Daniels, pp. 343-354. ASTM, 1982.

Barenblatt, G.I.: Dimensional Analysis. Gordon and Breach Science Publishers, NewYork, 1987.

Beldica, C.: Experimental and Numerical Analysis of Strength and Fracture in Fiber Composites. Ph.D. dissertation, University of Illinois at Chicago, Chicago, 1996.

Botsis, J., Beldica, C., and Zhao, D.: On strength scaling of composites with long aligned fibers. Intl. J. Fracture 68:375-384, 1995.

Botsis, J. and Beldica, C.: Strength characteristics and fatigue crack growth in a composite with long aligned fibers. Intl. J. Fracture 69:27-50, 1994-95.

Botsis, J., Beldica, C., and Zhao, D.: Strength and fracture of composites with long aligned fibers. in Failure Mechanics in Advanced Polymeric Composites, AMD-Vol. 196, eds. G.A. Kardomateas and Y.D.S. Rajapakse, pp. 93-107, Chicago, 1994

Bouden A., Aboura, Z., Benzeggagh, M., and Lambertin, M.: Signal processing of acoustic emission for damage identification in woven composite materials. 1st Joint Belgian-Hellenic Conference on Nondestructive Testing, Patras, Greece, 1995.

Bradley, W.L. and Cohen, R.N., In: Delamination and Debonding of Materials; ASTM STP 876, ed. W.S. Johnson, pp. 448-464., Philadelphia, ASTM, 1983.

Broutman, L.J. and Krock, R.H.: Modern Composite Materials. Reading, Addison-Wesley Publishing Co., 1967.

Budiansky, B., Hutchinson, J.W., and Evans, A.G.: Matrix fracture in fiber-reinforced ceramics. J. Mechanics of Physics and Solids 34:167- , 1986.

Bunsell, A.R.: In: Proc. First USA-USSR Symposium on Fracture of Composite Materials, eds. G.C. Sih and V.P. Tamzus, pp. 349-359. Alphen aan den Rijn, Sijthoff and Noordhoff, 1978.

Carniglia, S.C.: Re-examination of experimental strength-vs-grain size data for ceramis. J. Am. Ceramic Society 55:No.5:243-249, 1972.

Cofer, C.G., Economy, J., Xu, Y., and Zangvil, A.: Characterization of interfaces in boron nitride matrix composites. University of Illinois at Champaign-Urbana Dept. of Material Science and Engineering Report, NSF Grant (DMR 9411757), 1995.

Cohen, J. and Awerbuch, J.: Monitoring delamination progression in composites through acoustic emission during fatigue loading. In: Proc. 4th Japan-U.S. Conf. Composite Materials, pp. 1035-1046, Lancaster, Technomic Publishing Co., Inc., 1988.

Cook, J. and Gordon, E.: Proc. Roy. Soc. London A282:508-520, 1964.

Corten, H.T.: Micromechanics and fracture behavior of composites. In: Modern Composite Materials. Eds. L.J. Broutman and R.H. Krock, pp. 27-105, 1967.

Czigany, T. and Karger-Kocsis, J.: Comparison of the failure mode in short and long glass fiber-reinforced injection-molded polypropylene composites by acoustic emssion. Polymer Bulletin 31:495-501, 1993.

Daniel, I.M.: Composite materials. In: Handbook on Experimental Mechanics, ed. A.S. Kobayashi, pp. 829-904. New York, VCH Publishers Inc., 1993

Davidge, R.W.: The mechanical properties and fracture behavior of ceramic matrix composites (CMC) reinforced with continuous fibers. In: Application of Fracture Mechanics to Composite Materials : Composite Materials Series. Vol. 6, ed. K. Friedrich, pp. 547-570, Elsevier, New York, 1989.

Davidson, B.D.: Prediction of delamination growth in laminated structures. in Failure Mechanics in Advanced Polymeric Composites, AMD-Vol. 196, eds. G.A. Kardomateas and Y.D.S. Rajapakse, pp. 43-66, Chicago, 1994

Evans, A.G. and Davidge, R.W.: The strength and fracture of fully dense polycrystalline magnesium oxide. The Philosophical Magazine 20:373-388, 1969.

Griffith A.A.: Phil. Trans. Roy. Soc. A22:163-198, 1921

Gustafson, C.G. and Selden, R.B: In Delamination and Debonding of Materials: ASTM STP 876, ed. W.S. Johnson, pp. 448-464., Philadelphia, ASTM, 1983.

Hull, D.: An Introduction to Composite Materials. Cambridge, Press syndicate of Cambridge University, 1981.

Johannesson, J. and Blikstad, M.: Mixed mode fracture in graphite/epoxy laminates. Composites Science and Technology. Vol. 24:No.1:33-46, 1985

Kardomateas, G.A., Pelegri, A.A., and Malik, B.: Growth of internal delaminations under cyclic compression in composite plates. In Failure Mechanics in Advanced Polymeric Composites, AMD-Vol. 196, eds. G.A. Kardomateas and Y.D.S. Rajapakse, pp. 13-30, Chicago, 1994

Kerans, R.J. and Parthasarathy, J.A.: Theoretical analysis of the fiber pull-out and push-out tests. J. Am. Ceramic Soc. 74:No.7:1585-96, 1991.

69

Kerans, R.J., Hay, R.S., Pagano, N.J., and Parthasarathy, J.A.: The role of the fiber-matrix interface in ceramic composites. Ceramic Bulletin 68:No.2:429-442, 1989.

Kim, R.Y. and Pagano, N.J.: Crack initiation in unidirectional brittle-matrix composites. J. Am. Ceramic Soc. 74:No.5:1082-1090, 1991.

Kingery, W.D., Bowen, H.K., and Uhlmann, D.R.: Introduction to Ceramics John Wiley and Sons, New York, 1976.

Ko, F.K.: Preform fiber architecture for ceramic-matrix compostites. Ceramic Bulletin 68:No.2:401-414, 1989.

Kuich, G.: The boundary element method in an industrial environment. In Boundary Element Methods in Engineering. ed. C.A. Brebbia, Springer-Verlag, Berlin, 1982.

Lackman W.L.: In: Proc. First USA-USSR Symposium on Fracture of Composite Materials, eds. G.C. Sih and V.P. Tamzus, pp. 395-410. Alphen aan den Rijn, Sijthoff and Noordhoff, 1978.

Lathishenko, V.A. and Matiss, I.G.: In: Proc. First USA-USSR Symposium on Fracture of Composite Materials, eds. G.C. Sih and V.P. Tamzus, pp. 321-328. Alphen aan den Rijn, Sijthoff and Noordhoff, 1978.

Marshall, D.B., Cox, B.N., and Evans A.G.: Mechanics of matrix cracking in brittle-matrix fiber composites. Acta. Metall. 33:No.11:2013-2021, 1985.

Parikh, N.M.: Deformation and fracture modes in fiber-reinforced metals. In: Fiber Composite Materials ASM, 1964.

Pollock, A.A.: AE inspection. In: Metals Handbook, 9th Ed., Vol. 17, pp. 278-294, ASM Intl., 1989.

Prewo, K.M.: Fiber-reinforced ceramics: New opportunities for composite materials. Ceramic Bulletin 68:No.2:395-400, 1989.

Priston, A.M., Hill, R., and Brooks, R.: Damage prediction using associated acoustic emission from composite material. 1st Joint Belgian-Hellenic Conference on Nondestructive Testing. Patras. Greece, 1995.

Rice, R.W.: Strength/grain size effects in ceramics. Proc. British Cermamic Society 20:205-257, 1972.

Rosakis, A.J., Lambros, J., and Karyeaclis, M.P.: Experimental investigation of dynamic delamination in thick polymeric composite laminates. in Failure Mechanics in Advanced Polymeric Composites, AMD-Vol. 196, eds. G.A. Kardomateas and Y.D.S. Rajapakse, pp. 1-12, Chicago, 1994

Rosen, B.W.: In: Fiber Composite Materials ASM, 1964.

Rubinstein, A.A.: Strength of fiber reinforced ceramics on the basis of micro-mechanical analysis, J. Mech. Phys. Solids. Vol.42:No.3:410-422, 1993.

Schuster, J. and Steiner, K.V.: Ultrasonic backscattering using digitized full-waveform scanning technique. J. Composites Technology and Research 15:No.2:143-148 , 1993.

Shah, S.P. and Oyang, C.: Mechanical behavior of fiber-reinforced cement-based composites, J. Amer. Ceramic Soc. Vol.74:No.11:2727-2738, 2947-2953, 1991.

Shibata, S., Mori, T., and Mura, T.: Crack arrest in a composite reinforced by long sliding fibers. In: Proc. 4th Japan-U.S. Conf. Composite Materials, pp. 975-980, Lancaster, Technomic Publishing Co., Inc., 1988.

Smith, C.W. and Kobayashi, A.S.: Experimental fracture mechanics. In: Handbook on Experimental Mechanics, ed. A.S. Kobayashi, pp. 905-968. New York, VCH Publishers Inc., 1993

Sou, Z., Wu., B., and He, M.-Y.: Notch sensitivity and shear bands in brittle matrix composites, Acta Metall. Mater. Vol.42:No.9:3065-3070, 1994

Sun, C.T. and Chu, G.D.: In: Proc. 4th Japan-U.S. Conf. Composite Materials, pp. 515-527, Lancaster, Technomic Publishing Co., Inc., 1988.

Sundaresan, M.J. and Henneke, E.G. II: Failure Processes in unidirectional composite materials: Comparison of different composite systems, In: Proc. 4th Japan-U.S. Conf. Composite Materials pp. 1001-1005, Lancaster, Technomic Publishing Co., Inc., 1988.

Tada, H.: The Stress Analysis of Cracks Handbook. Hellertown, Del Research Corp., 1973.

Timoshenko, S.: Strength of Materials, Part II Advanced Theory and Problems. Princeton, D. Van Nostrand Co., 1956.

Tittman, B.R.: Ultrasonic measurements for the prediciton of mechanical strength. NDT Intl. Feb:17-22, 1978.

Vahaviolos, S.J.: Acoustic emission: A new but sound NDE technique not a panacea. 1st Joint Belgian-Hellenic Conference on Nondestructive Testing, Patras, Greece (copyright Physical Acoustics Corp., Princeton), 1995.

Wagner, H.D.: Statistical concepts in the study of fracture properties of fibers and composites. In: Application of Fracture Mechanics to Composite Materials : Composite Materials Series, Vol. 6. ed. K. Friedrich, pp. 39-81, Elsevier, New York, 1989.

Warren, R. and Sarin, V.K.: Fracture in whisker-reinforced ceramics. In: Application of Fracture Mechanics to Composite Materials : Composite Materials Series, Vol. 6, ed. K. Friedrich, pp. 571-614, Elsevier, New York, 1989.

Wearing, J.L., Sheikh, M.A., and Rahmani, O.: A combined finite element-boundary element approach for three-dimensional stress analysis. In Boundary Elements in Mechanical and Electrical Engineering. eds. C.A. Brebbia and A. Chaudouet-Miranda, Computationl Mechanics Publications, Boston, 1990

Zhao, D.: Strength Characteristics and Fracture Behavior of Model Composites. Ph.D. dissertation, University of Illinois at Chicago, Chicago, 1995.

Zong-Fu Li and Grubb, D.T.: Single-fiber polymer composites: Part I Interfacial shear strength and stress distribution in the pull-out test. J. Materials Science 29:189-202, 1994.

LIST OF PROFESSIONAL PERSONNEL AND PUBLICATIONS

PERSONNEL: John Botsis, Professor

                 Kevin Gaffney (US Citizen), MS Completed, November 1996

PUBLICATIONS

The results of this project are being prepared for two Journal Publications:

1.   K. Gaffney and J. Botsis 'Influence of the fiber spacing on strength and fracture: Part I - monolayer system'

2.   K. Gaffney and J. Botsis 'Influence of the fiber spacing on strength and fracture: Part II - multilayer system'